Axisymmetric Simulations of Rotating Stellar Collapse in Full General Relativity

—— *Criteria for Prompt Collapse to Black Holes* ——

Masaru SHIBATA

Department of Physics, University of Illinois at Urbana-Champaign
Urbana, IL 61801, USA
Department of Earth and Space Science, Graduate School of Science
Osaka University, Toyonaka 560-0043, Japan

Motivated by a recent paper by the Potsdam numerical relativity group, we have constructed a new numerical code for hydrodynamic simulation of axisymmetric systems in full general relativity. In this code, we solve the Einstein field equation using Cartesian coordinates with appropriate boundary conditions. On the other hand, the hydrodynamic equations are solved in cylindrical coordinates. Using this code, we perform simulations to study axisymmetric collapse of rotating stars, which thereby become black holes or new compact stars, in full general relativity. To investigate the effects of rotation on the criterion for prompt collapse to black holes, we first adopt a polytropic equation of state, $P = K\rho^{\Gamma}$, where P, ρ, and K are the pressure, rest mass density, and polytropic constant, with $\Gamma = 2$. In this case, the collapse is adiabatic (i.e., no change in entropy), and we can focus on the bare effect of rotation. As the initial conditions, we prepare rigidly and differentially rotating stars in equilibrium and then decrease the pressure to induce collapse. In this paper, we consider cases in which $q \equiv J/M_g^2 < 1$, where J and M_g are the angular momentum and the gravitational mass. It is found that the criterion of black hole formation is strongly dependent on the angular momentum parameter q. For $q < 0.5$, the criterion is not strongly sensitive to q; more precisely, if the rest mass is slightly larger than the maximum allowed value of spherical stars, a black hole is formed. However, for $q \lesssim 1$, it changes significantly: For $q \simeq 0.9$, the maximum allowed rest mass becomes ~ 70–80% larger than that for spherical stars. These findings depend only weakly on the rotational profiles given initially. We then report the results for simulations employing a Γ-law equation of state $P = (\Gamma - 1)\rho\varepsilon$, where ε is the specific internal energy, to study effects of shock heating. We find that the effects of shock heating are particularly important for preventing prompt collapse to black holes in the case of large q [i.e., $q = O(1)$].

§1. Introduction

In the 1980s, one of the most important issues in numerical relativity was to perform simulations of rotating stellar collapse with the assumption of axial symmetry. It seems that there were two motivations for such studies. [1] One was to explore the final fate after gravitational collapse of rotating stars. If the cosmic censorship conjecture suggested by Penrose [2] is correct, any collapsed star should be surrounded by an event horizon, and consequently settle down to a rotating Kerr black hole, according to the uniqueness theorem of Israel, [3] Carter [4] and others. [5] However, if this conjecture is not correct, such a star might be reduced to a state with naked singularities. Numerical relativity was required to resolve this problem. The other motivation was to compute gravitational wave forms in the collapse, because the

gravitational collapse of a rotating star to a black hole or a neutron star is one of promising sources of gravitational waves.

Simulations of rotating stellar collapse in full general relativity were first performed by Nakamura.[6] Using the (2+1)+1 formalism developed by Maeda et al.,[7] he performed simulations of rotating collapse for massive stars whose masses are much larger than the maximum allowed mass for neutron star formation. He used cylindrical coordinates (ϖ, z) with a non-uniform grid spacing. At that time, he was able to use at most a (42,42) grid resolution for (ϖ, z) because of restricted computational resources. The interesting finding in his simulations was that the rotational parameter $q \equiv J/M_g^2$, where J and M_g are the angular momentum and gravitational mass, can be an important parameter for determining black hole formation: The results of his simulations suggest that if $q > 1$, no black hole is formed, indicating that cosmic censorship holds. Unfortunately, he was not able to compute gravitational waves, because his computational resources were severely restricted and the formalism he used was not well suited for computing gravitational wave forms in the wave zone.

To compute gravitational waves emitted during gravitational collapse to black holes, Stark and Piran[8] performed simulations similar to those of Nakamura, adopting spherical polar coordinates with a typical grid size $(100, 16)$ for (r, θ). The distinguishing feature of their work is that they adopted the Bardeen-Piran formalism,[9] which is well suited for computation of gravitational waves in the wave zone. As a result of this choice of formalism, they succeeded in computing gravitational wave forms, and clarified that the wave forms are characterized by the quasi-normal mode of rotating black holes formed after gravitational collapse and that the total radiated energy of gravitational waves is at most 0.1% of the gravitational mass of the system.[8]

Since the completion of their work, no new work in this field has been done for about 15 years.[10] Although several questions they originally wished to answer have been answered by their simulations, there are still many unsolved issues in astrophysics and general relativity that can be investigated using axisymmetric hydrodynamic simulations in full general relativity. For example, the following issues should be addressed as open questions: (1) Previous simulations were performed using restricted initial conditions and equations of state.[6],[8] It is not clear whether their results are independent of the initial velocity field, density profile, internal energy distribution, and equations of state. A systematic study considering different initial settings should be carried out for detailed exploration of the validity of the cosmic censorship conjecture. (2) Previous works have indicated that if $q > 1$, a black hole is not formed. However, these works did not carefully investigate how the criterion of black hole formation changes due to the effect of rotation for $q < 1$. (3) Stark and Piran computed gravitational wave forms in the case of black hole formation. There have been also many Newtonian works for computing gravitational wave forms in the formation of neutron stars that are not very massive and compact.[11] However, there has been no fully general relativistic work for computing gravitational wave forms in neutron star formation. For the case in which the formed neutron star is so massive and compact that general relativistic effects play

an important role even at the formation, fully general relativistic studies on gravitational waves could contribute to the understandings of gravitational-wave-astronomy. (4) Realistic simulations of the rotating collapse of massive stars, which thereby become black holes (or proto-neutron stars) in full general relativity, have not yet been performed. This should be done to understand mechanisms of black hole formation in nature. Actually, a study of the formation of rapidly rotating black holes with surrounding accretion disks in stellar core collapse is currently one of the hot topics in connection with a hypothetical scenario for the central engine of γ-ray bursts. [12] (5) The formation mechanism of supermassive black holes of mass 10^6–$10^9 M_\odot$, where $M_\odot$ denotes the solar mass, is also an open issue. Recently, Baumgarte and Shapiro have proposed an interesting scenario in which rigidly rotating supermassive stars at mass-shedding limits (i.e., rigidly rotating stars of maximum rotational velocity) are possible progenitors of supermassive black holes. [13] According to their scenario, after dissipating the internal energy due to thermal radiation, the supermassive stars become unstable at the point at which $R/M_g \sim 450$ and $q \simeq 0.97$, where R denotes the circumferential radius at the equator. Since $q \sim 1$, it is not clear whether such a progenitor really collapses to a black hole. To confirm that the scenario is promising, simulation in full general relativity is necessary.

All these arguments obviously remind us that there are still many astrophysical and general relativistic motivations for performing hydrodynamic simulations of the rotating collapse of massive and supermassive stars in full general relativity.

Before proceeding, we roughly summarize the present situation regarding our computational resources. Recently, we have been performing 3D numerical simulations in full general relativity with Cartesian coordinates (x, y, z) for investigating merging processes of binary neutron stars. [14], [15] Our 3D simulations are performed on the FACOM VPP/300R at the National Astronomical Observatory of Japan (NAOJ), in which we can use about 30 GBytes memory. We assume a plane symmetry with respect to the equatorial plane ($z = 0$) and use a grid of size $(2N + 1, 2N + 1, N + 1)$ in (x, y, z) where N is at most 160. Let us here estimate a desirable grid number N for simulation of the merging of binary neutron stars. In the following, we assume to use a uniform grid.

First, we wish to locate the outer boundary in the wave zone to compute the gravitational wave forms accurately. The typical wavelength of gravitational waves just before the merging of two neutron stars is about $50M_g$. Thus, the outer boundaries should be located for $> 50M_g$. Second, such a binary could result in a black hole, and to resolve the black hole formation accurately, we need at least 10 grid points in the gravitational radius $\sim M_g$. These considerations imply that if we use a uniform grid, we need $N > 500$ for an accurate computation. In the next generation machines, which will be available in a year, we will be able to use several hundred GBytes. In this case, $N = 400(\text{Memory}/400\ \text{GBytes})^{1/3}$ would be feasible. This is close to the value needed for accurate computation. However, with this maximum number, it would take ~ 100 CPU hours for one simulation on such machines, in which the computational speed is several hundred GFlops. This implies that a *systematic survey*, performing simulations for $\lesssim 100$ models of different equations of state and compactness of neutron stars, would still be a difficult task to complete on

a time scale of approximately a year. (Note that under normal circumstances, we can use at most ~ 1000 CPU hours per year.)

In contrast, the memory and computational speed of present computational resources are large enough for axisymmetric simulations with $\sim (500, 500)$. In the following, we assume the use of cylindrical coordinates (ϖ, z), with reflection symmetry with respect to $z = 0$; i.e., the computational domain is assumed to be in the region satisfying $0 \le \varpi \le L_x$ and $0 \le z \le L_z$, where L_x and L_z are constants. In this case, a simulation with grid size $\sim (500, 500)$ can be performed on a machine with $\lesssim 1$ GBytes and ~ 1 GFlops using only ~ 10 CPU hours or less (see below). This implies that a systematic survey performing simulations for ~ 100 models with $N \sim 500$ can be completed for axisymmetric systems in several months. Using more powerful machines, such as FACOM VPP/300R, we could use grids of size about $(3000, 3000)$. In this case, completion of highly-resolved simulations would also be feasible.

One longstanding problem for axisymmetric simulations in full general relativity has been to develop methods in which the accuracy and stability for a long-duration simulation can be preserved. In axisymmetric simulations, we have in general used cylindrical and spherical coordinate systems, which have coordinate singularities at the origin and along the symmetric axis $\varpi = 0$. At such singularities, we have often faced several troubles. For example, there appear singular terms in the (3+1) form of the Einstein equation, such as [1]

$$\frac{\gamma_{\varpi\varpi,\varpi}}{\varpi} \quad \text{and} \quad \frac{1}{\varpi^2}\left(\gamma_{\varpi\varpi} - \frac{\gamma_{\varphi\varphi}}{\varpi^2}\right), \tag{1.1}$$

where γ_{ij} denotes the three metric. Because of the regularity condition along the symmetric axis $\varpi = 0$, these terms are finite in reality, but it is necessary to introduce appropriate prescriptions to guarantee them to be finite. Moreover, at the coordinate singularities, we have to change the scheme for finite differencing, because there are no negative value of ϖ and r. Under such changes, the numerical system can have a mismatching between the coordinate singularities and their neighborhoods, often resulting in the accumulation of numerical error and, thus, numerical instability. For a long-duration simulation, we have often been required to add artificial viscosities around the coordinate singularities to stabilize the numerical system. [16]

Recently, the Potsdam numerical relativity group has proposed a method to make a robust code for solving the Einstein field equation for axisymmetric systems. [17] The essence of their idea is that Cartesian coordinates could be used even for axisymmetric systems if the Einstein field equation is solved only for $y = 0$ (or $x = 0$), using the boundary condition at $y = \pm \Delta y$ (or $x = \pm \Delta x$) provided by the axial symmetry. Since the Einstein field equation is written in the Cartesian coordinate system, we neither have singular terms nor have to change the finite differencing scheme anywhere, except at the outer boundaries. Thus, it is possible to perform a stable and accurate, long-duration simulation without any prescription or artificial viscosities. Another merit for us is that it is easy to construct such a code, because we have already possessed a 3D code and only need to modify its boundary conditions.

Using this method, we have constructed a new numerical code for axisymmetric spacetimes and performed simulations of rotating stellar collapse. As a first step, in this paper, we focus on simulations adopting simple initial conditions and simple equations of state to investigate the effects of rotation on the criteria for prompt collapse to black holes. As initial conditions, we prepare rigidly and differentially rotating stars in equilibrium states which are not too compact. We prepare a large number of equilibrium states that have different values of q but identical values of the rest mass. Then, we reduce the pressure to induce gravitational collapse. We pay particular attention to collapse for $q < 1$ in this paper [i.e., we focus on the issue (2) mentioned above], because black holes are not likely to be formed for $q > 1$.[6),8)] For most computations, we adopt a polytropic equation of state [see Eq. (2·2)]; namely, we do not take into account the effect of shock heating. In this treatment, it is easy to investigate the bare effect of rotation for black hole formation. For some computations, we adopt a Γ-law equation of state [see Eq. (2·3)] to investigate the effect of shock heating. To roughly mimic a moderately stiff equation of state for neutron stars, the adiabatic constant Γ is set to 2. Giving the numerical results for this experiment, we demonstrate that our present strategy and current computational resources are sufficient to systematically perform stable and well-resolved hydrodynamic simulations in axisymmetric numerical relativity.

The paper is organized as follows. In §2 we describe the formulation and numerical methods. In §3 we give the initial conditions which we adopt in this paper. In §4 we present the numerical results. Section 5 is devoted to summary and discussion. Throughout this paper, we adopt units in which $G = 1 = c$, where G and c denote the gravitational constant and speed of light. We use Cartesian coordinates, $x^k = (x, y, z)$ as the spatial coordinates, with $r = \sqrt{x^2 + y^2 + z^2}$, $\varpi = \sqrt{x^2 + y^2}$ and $\varphi = \tan^{-1}(y/x)$. t denotes the coordinate time. In the following, we use a uniform grid with grid spacing $\Delta x = \Delta y = \Delta z$ or $\Delta x = \Delta y = 2\Delta z$. Greek indices $\mu, \nu, \cdots$ denote x, y, z and t, small Latin indices $i, j, k, \cdots$ denote x, y and z, and capital Latin indices A and B denote x and z.

§2. Methods

2.1. *Summary of formulation*

For solving the Einstein field equation, we use the same formulation and gauge condition as in Refs. 18), 14) and 19), to which the reader may refer for details and basic equations. The fundamental variables for the geometry used in this paper are as follows:

$$\alpha : \text{lapse function},$$
$$\beta^k : \text{shift vector},$$
$$\gamma_{ij} : \text{metric in 3D spatial hypersurface},$$
$$\gamma = e^{12\phi} = \det(\gamma_{ij}),$$
$$\tilde{\gamma}_{ij} = e^{-4\phi}\gamma_{ij},$$
$$K_{ij} : \text{extrinsic curvature}.$$

The variables, $\tilde{\gamma}_{ij}$, ϕ, $\tilde{A}_{ij} \equiv e^{-4\phi}(K_{ij} - \gamma_{ij}K_k{}^k/3)$, together with the three auxiliary functions $F_i \equiv \delta^{jk}\partial_k\tilde{\gamma}_{ij}$ and the trace of the extrinsic curvature $K_k{}^k$, evolve according to a free evolution code.

As the matter source of the Einstein equation, we use an ideal fluid. The fundamental variables are defined as follows:

$$\rho : \text{rest mass density,}$$
$$\varepsilon : \text{specific internal energy,}$$
$$P : \text{pressure,}$$
$$h = 1 + \varepsilon + P/\rho,$$
$$u^\mu : \text{four velocity; } \hat{u}_k = hu_k,$$
$$v^k = \frac{u^k}{u^0}; \ \Omega = v^\varphi,$$
$$w = \alpha u^0 = \sqrt{1 + \gamma^{ij}u_iu_j}. \tag{2.1}$$

In this paper, we adopt two kinds of equations of state for the dynamical simulations. One is a polytropic equation of state,

$$P = K\rho^\Gamma, \tag{2.2}$$

where K is fixed to a constant value throughout the evolution. The other is a Γ-law equation of state of the form

$$P = (\Gamma - 1)\rho\varepsilon. \tag{2.3}$$

In both cases, we set the adiabatic constant as $\Gamma = 2$ (i.e., the polytropic index n is given by $n = 1/(\Gamma - 1) = 1$) as a qualitative approximation of moderately stiff equations of state for neutron stars. We note that if we prepare a polytropic star as the initial conditions and the system evolves in an adiabatic manner without shocks, the equation of state is preserved in the form of Eq. (2.2), even using Eq. (2.3); i.e., the value $P/\rho^\Gamma \equiv K'(x^\mu)$ for any fluid element remains a constant $(= K)$.

In the simulation with the equation of state (2.2), the entropy of each fluid element is conserved during the time evolution. For this reason, we refer to the collapse with Eq. (2.2) as "adiabatic collapse" in the following.

The slicing and spatial gauge conditions we use in this paper are basically the same as those adopted in our previous series of papers; [18], [14], [19] i.e., we impose an "approximate" maximal slice condition ($K_k{}^k \simeq 0$) and an "approximate" minimum distortion (AMD) gauge condition ($\tilde{D}_i(\partial_t\tilde{\gamma}^{ij}) \simeq 0$, where $\tilde{D}_i$ is the covariant derivative with respect to $\tilde{\gamma}_{ij}$). For the case in which a rotating star significantly contracts and ϕ increases by a large factor, we slightly modify the spatial gauge condition in order to improve the spatial resolution around the highly relativistic region, as in Refs. 18) and 19). In this paper, we modify the gauge according to

$$\beta^x = \beta^x_{\text{AMD}} - f(t)\frac{x}{\varpi + \epsilon}\beta^{\varpi'}_{\text{AMD}}, \tag{2.4}$$

$$\beta^y = \beta^y_{\text{AMD}} - f(t)\frac{y}{\varpi + \epsilon}\beta^{\varpi'}_{\text{AMD}}, \tag{2.5}$$

$$\beta^z = \beta^z_{\text{AMD}}[1 - f(t)], \tag{2.6}$$

where ϵ is a constant much less than Δx and Δz, β^k_{AMD} is β^k in the AMD gauge condition, $\beta^{\varpi'}_{\mathrm{AMD}} = (\beta^x_{\mathrm{AMD}}x + \beta^y_{\mathrm{AMD}}y)/(\varpi + \epsilon)$, and $f(t)$ is chosen as

$$f(t) = \begin{cases} 1 & \text{for } \phi_0 \geq 1.0, \\ 2\phi_0 - 1 & \text{for } 0.5 \leq \phi_0 \leq 1.0, \\ 0 & \text{for } \phi_0 < 0.5, \end{cases} \tag{2·7}$$

where ϕ_0 is ϕ at $r = 0$. Namely, for large $\phi_0 \geq 1$, $\beta^z = 0$ and $\beta^\varpi \simeq 0$, but $\beta^\varphi \neq 0$.

We impose axial symmetry, following Ref. 17). First, we define the computational domain as $0 \leq x, z \leq L$ and $-\Delta y \leq y \leq \Delta y$, where L denotes the location of the outer boundaries, and reflection symmetry with respect to the $z = 0$ plane is assumed. In this computational domain, we need only 3 points in the y direction, 0 and $\pm\Delta y$. We here determine that the Einstein equation is solved only in the $y = 0$ plane. Then, the boundary conditions at $y = \pm\Delta y$ that are necessary in evaluating y-derivatives are supplied from the assumption of axial symmetry as

$$Q_{xx} = Q^{(0)}_{xx}\cos^2\varphi - Q^{(0)}_{xy}\sin 2\varphi + Q^{(0)}_{yy}\sin^2\varphi,$$

$$Q_{xy} = \frac{1}{2}Q^{(0)}_{xx}\sin 2\varphi + Q^{(0)}_{xy}\cos 2\varphi - \frac{1}{2}Q^{(0)}_{yy}\sin 2\varphi,$$

$$Q_{yy} = Q^{(0)}_{xx}\sin^2\varphi + Q^{(0)}_{xy}\sin 2\varphi + Q^{(0)}_{yy}\cos^2\varphi,$$

$$Q_{xz} = Q^{(0)}_{xz}\cos\varphi - Q^{(0)}_{yz}\sin\varphi, \qquad Q_{yz} = Q^{(0)}_{xz}\sin\varphi + Q^{(0)}_{yz}\cos\varphi,$$

$$Q_x = Q^{(0)}_x\cos\varphi - Q^{(0)}_y\sin\varphi, \qquad Q_y = Q^{(0)}_x\sin\varphi + Q^{(0)}_y\cos\varphi,$$

$$Q_{zz} = Q^{(0)}_{zz}, \qquad Q_z = Q^{(0)}_z, \qquad Q = Q^{(0)},$$

where $\varphi = \varphi(x) = \tan^{-1}[\pm\Delta y/\sqrt{x^2 + (\Delta y)^2}]$, Q_{ij}, Q_i and Q are an arbitrary tensor, vector and scalar in the 3D spatial hypersurface, and $Q^{(0)}_{ij}, Q^{(0)}_i$ and $Q^{(0)}$ denote the values of Q_{ij}, Q_i and Q at $(\sqrt{x^2 + (\Delta y)^2}, 0, z)$, which are interpolated using Lagrange's formula [20] with three nearby points along the x direction (i.e., $x \pm \Delta x$ and x). At $x = L$, we use only two points, $x - \Delta x$ and x, for the extrapolation. We note that in using the interpolation and extrapolation, we assume that the geometric variables are smooth functions. This assumption is justified as long as black holes are not formed. In the case of black hole formation, however, some of the geometric variables around the black hole horizons become very steep. In such a situation, the interpolation (and extrapolation) becomes less accurate.

To impose the gauge conditions, as well as to solve constraint equations in preparing the initial conditions, we solve scalar and vector elliptic-type equations of the form [14]

$$\Delta Q = S, \tag{2·8}$$

$$\Delta Q_i = S_i, \tag{2·9}$$

where Δ denotes the Laplacian in the flat 3D space, and S and S_i denote the source terms. Using the interpolation mentioned above, $\partial_{yy}Q$ and $\partial_{yy}Q_i$ are evaluated in the finite differencing as

$$\partial_{yy}Q = 2\frac{Q^{(0)} - Q(x, 0, z)}{(\Delta y)^2}, \qquad \partial_{yy}Q_z = 2\frac{Q^{(0)}_z - Q_z(x, 0, z)}{(\Delta y)^2},$$

$$\partial_{yy}Q_x = 2\frac{Q_x^{(0)}|\cos\varphi| - Q_x(x,0,z)}{(\Delta y)^2}, \quad \partial_{yy}Q_y = 2\frac{Q_y^{(0)}|\cos\varphi| - Q_y(x,0,z)}{(\Delta y)^2}.$$

On the other hand, the finite differencing in the x and z directions, $\partial_{xx}Q_i$ and $\partial_{zz}Q_i$, are written in the standard form as

$$\frac{Q_i(x+\Delta x,0,z) - 2Q_i(x,0,z) + Q_i(x-\Delta x,0,z)}{(\Delta x)^2},$$

$$\frac{Q_i(x,0,z+\Delta z) - 2Q_i(x,0,z) + Q_i(x,0,z-\Delta z)}{(\Delta z)^2}.$$

Thus, in the finite differencing form for each component of Eq. (2·9), only one component of Q_i is included, implying that each component of the vector elliptic-type equation is solved independently, as in the case of the scalar elliptic equation.

For computation of hydrodynamic equations, on the other hand, we do not use the above method. Instead, we solve the equations in cylindrical coordinates. These equations are written in the $y = 0$ plane as

$$\partial_t \rho_* + \frac{1}{x}\partial_x(\rho_* x v^x) + \partial_z(\rho_* v^z) = 0, \tag{2·10}$$

$$\partial_t(\rho_* \hat{u}_A) + \frac{1}{x}\partial_x(\rho_* x \hat{u}_A v^x) + \partial_z(\rho_* \hat{u}_A v^z)$$
$$= \frac{\rho_* \hat{u}_y v^y}{x}\delta_{Ax} - \alpha e^{6\phi}\partial_A(P + P_{\text{art}})$$
$$- \rho_*\left[wh\partial_A\alpha - \hat{u}_j\partial_A\beta^j + \frac{\alpha e^{-4\phi}\hat{u}_i\hat{u}_j}{2wh}\partial_A\tilde{\gamma}^{ij} - \frac{2\alpha h(w^2-1)}{w}\partial_A\phi\right], \tag{2·11}$$

$$\partial_t(\rho_* \hat{u}_y) + \frac{1}{x^2}\partial_x(\rho_* x^2 \hat{u}_y v^x) + \partial_z(\rho_* \hat{u}_y v^z) = 0, \tag{2·12}$$

$$\partial_t e_* + \frac{1}{x}\partial_x(e_* x v^x) + \partial_z(e_* v^z) = \dot{e}_{\text{art}}, \tag{2·13}$$

where $\rho_* \equiv \rho w e^{6\phi}$ and $e_* \equiv (\rho\varepsilon)^{1/\Gamma}we^{6\phi}$. P_{art} and $\dot{e}_{\text{art}}$ denote artificial viscous terms, and are added in the same manner as those in Ref. 14) only for the Γ-law equations of state to consider effects of shock heating. Equations (2·10)–(2·13) represent the continuity equation, Euler equation for the x and z directions ($A = x$ or z), Euler equation for the y direction (or angular momentum equation), and energy (or entropy) equation, respectively. The hydrodynamic equations are solved using van Leer's scheme for the advection terms[21] in this paper. We note that for the polytropic equations of state (2·2), we do not have to solve Eq. (2·13)[22] nor add the artificial viscous terms.

There are two reasons why we adopt these equations instead of the equations in Cartesian coordinates. One is that in the simulation, conservation of the rest mass and angular momentum of the system during the evolution is easily guaranteed in these forms with help of standard numerical methods. The other is that the hydrodynamic variables often become non-smooth in the presence of shocks in contrast to the geometric variables. In such cases, the axisymmetric conditions imposed by the interpolation (and extrapolation) are less accurate.

With these axisymmetric equations, however, there exist coordinate singularities along the symmetric axis ($x = 0$) which might cause a numerical instability for a long-duration simulation. In order to avoid such instability, we here add small artificial viscous terms

$$\nu_{\mathrm{vis}} \rho_* \Delta \hat{u}_A \qquad (2\cdot14)$$

to Eq. (2·11) in order to stabilize the system. Here, Δ denotes the flat Laplacian again, and ν_{vis} is a small constant such that the typical dissipation time scale due to the viscosity, $(\Delta x)^2/\nu_{\mathrm{vis}}$, is much longer than the dynamical time scale of the system, $\sim \rho_c^{-1/2}$, where ρ_c denotes the central density at $t = 0$.

We note that there are no y-derivatives in Eqs. (2·10)–(2·13), so that we do not have to assign grid points at $\pm\Delta y$ for the hydrodynamic variables (i.e., we can save memory).

To check the accuracy of the numerical results, we monitor the conservation of the total rest mass M_*, gravitational mass M_g, and angular momentum J, which are computed in the $y = 0$ plane as

$$M_* = 4\pi \int_0^{L_x} x dx \int_0^{L_z} dz \rho_*, \qquad (2\cdot15)$$

$$M_g = -2 \int_0^{L_x} x dx \int_0^{L_z} dz \left[-2\pi E e^{5\phi} + \frac{e^\phi}{8} \tilde{R} - \frac{e^{5\phi}}{8} \left\{ K_{ij} K^{ij} - (K_k{}^k)^2 \right\} \right], \quad (2\cdot16)$$

$$J = 4\pi \int_0^{L_x} x^2 dx \int_0^{L_z} dz \rho_* \tilde{u}_y, \qquad (2\cdot17)$$

where $E = \rho h w^2 - P$ and $\tilde{R}$ is the Ricci scalar with respect to $\tilde{\gamma}_{ij}$. M_* should be conserved in all systems. Because of the axial symmetry, J should also be conserved. On the other hand, M_g should not be conserved because of gravitational radiation. However, the total radiated energy of gravitational waves is likely to be quite small in the axisymmetric spacetime, so that we can consider M_g as an approximately conserved quantity. We also monitor the conservation of the specific angular momentum spectrum [23]

$$M_*(j_0) = 4\pi \int_{j \le j_0} x dx dz \rho_*, \qquad (2\cdot18)$$

where j is the specific angular momentum computed as $x\hat{u}_y (= hu_\varphi)$ and j_0 denotes a particular value for j. We stop simulations before violation of the conservation of these quantities is large.

2.2. Test simulations

Following Ref. 14), we have performed several test simulations, such as the spherical collapse of a pressure-free dust to a black hole, radial oscillation of stable spherical stars, and quasi-radial oscillation of stable rotating stars. As in Ref. 14), we have confirmed that the collapse of dust can be accurately computed up to the formation of the apparent horizon and that the frequency of the fundamental mode for radial oscillation of spherical stars is obtained. We have also checked that the frequency of the fundamental mode for quasi-radial oscillation of rapidly rotating

stars agrees with that computed in Refs. 14) and 19). From these results, we are convinced that our axisymmetric code is sufficiently robust to perform long-duration simulations stably and to provide reliable results.

§3.   Initial conditions for rotating stars

Initial conditions are prepared in the following manner. First, we adopt rigidly as well as differentially rotating stars in (approximately) equilibrium states using the polytropic equation of state $P = K_{\mathrm{i}}\rho^{\Gamma}$, with $\Gamma = 2$ and $K_{\mathrm{i}} = 1$. Approximate equilibrium states are obtained by choosing a conformally flat spatial metric, i.e., assuming $\gamma_{ij} = e^{4\phi}\delta_{ij}$. (See, e.g., Ref. 14) for the equations to be solved.) This approach is computationally convenient, and, as illustrated in Ref. 24), it provides an excellent approximation to exact equilibrium configurations. In particular, we here prepare equilibrium states which are not very compact, so that effects of the neglected spatial components of the metric are not important. Hence, the approximate initial conditions can be almost exact equilibrium states. We also note that this approach provides valid initial data for full general relativistic simulations in the sense that the solution satisfies the constraint equations exactly.

Following previous studies, [25)] we fix a differentially rotational profile according to

$$F(\Omega) \equiv u^0 u_{\varphi} = A^2(\Omega_0 - \Omega), \tag{3.1}$$

where A is an arbitrary constant which describes the length scale over which Ω changes, and Ω_0 is the angular velocity on the rotational axis. In this paper, A is chosen to be $\varpi_e/3$ and ϖ_e, where ϖ_e denotes the coordinate radius of rotating stars at the equator. In the Newtonian limit $u^0 \to 1$ and $u_{\varphi} \to \varpi^2\Omega$, the rotational profile reduces to

$$\Omega = \Omega_0 \frac{A^2}{\varpi^2 + A^2}. \tag{3.2}$$

Thus, for $A = \varpi_e/3$ and ϖ_e, Ω at $\varpi = \varpi_e$ (hereafter referred to as Ω_e) is about one tenth and half of Ω_0, respectively (cf. Tables II and III). Note that for $A \to \infty$, the rotational profile approaches the rigid rotation.

We prepare a large number of equilibrium states, changing the angular momentum parameter of the system, q, but fixing the rest mass M_* to 0.05.   In Tables

Table I.   Central density ρ_c, gravitational mass M_g, $q \equiv J/M_g^2$, T/W, R/M_g (where R is the circumferential radius at the equator), angular velocity Ω, and ratio of polar coordinate radius to equatorial radius (R_{ratio}) for rigidly rotating stars. M_* is fixed to 0.05, and the polytropic constant K is fixed to 1.

ρ_c	M_g	q	T/W	R/M_g	Ω	R_{ratio}	Model
0.018750	0.04909	0.978	0.0715	30.04	0.0892	0.717	(B)
0.019316	0.04907	0.902	0.0628	29.07	0.0861	0.750	(C)
0.020757	0.04903	0.702	0.0411	27.02	0.0748	0.833	(D)
0.022179	0.04899	0.473	0.0200	25.40	0.0557	0.917	(E)
0.022868	0.04898	0.327	0.00986	24.70	0.0403	0.958	(F)
0.023408	0.04897	0.143	0.00194	24.19	0.0183	0.992	(G)

Table II. The same as Table I, but for differentially rotating stars with $A = \varpi_e/3$. The rest mass is also fixed to 0.05. $\rho_{\max}$, instead of ρ_c, is given in the first column. In the sixth column, Ω_0 and Ω_e are given.

$\rho_{\max}$	M_g	q	T/W	R/M_g	(Ω_0, Ω_e)	R_{ratio}	Model
0.015286	0.04910	0.900	0.0767	27.51	(0.3668,0.0334)	0.650	(H)
0.017432	0.04905	0.715	0.0528	26.31	(0.3611,0.0329)	0.750	(I)
0.020327	0.04901	0.487	0.0268	25.14	(0.2470,0.0223)	0.867	(J)
0.022776	0.04897	0.230	0.00640	24.32	(0.1265,0.0114)	0.967	(K)

Table III. The same as Table II, but for differentially rotating stars with $A = \varpi_e$. The rest mass is also fixed to 0.05.

$\rho_{\max}$	M_g	q	T/W	R/M_g	(Ω_0, Ω_e)	R_{ratio}	Model
0.018646	0.04907	0.893	0.0635	27.76	(0.1239,0.0580)	0.767	(L)
0.020153	0.04904	0.717	0.0438	26.50	(0.1096,0.0512)	0.833	(M)
0.021913	0.04900	0.478	0.0210	25.18	(0.0813,0.0379)	0.917	(N)
0.023066	0.04897	0.252	0.00610	24.38	(0.0458,0.0213)	0.975	(O)

I–III, several quantities which characterize the properties of rotating stars are listed for $A = \infty$ (rigid rotation), $A = \varpi_e/3$, and $A = \varpi_e$. Here, the rotational kinetic energy T and the gravitational binding energy $W(> 0)$ are defined as

$$T = \frac{1}{2} \int \rho_* j \Omega d^3 x, \tag{3·3}$$

$$W = \int \rho_* \varepsilon d^3 x + T + M_* - M_g. \tag{3·4}$$

We note that for unit in which $K_i = 1$, the maximum allowed rest masses of spherical stars (hereafter $\bar{M}_{*\mathrm{smax}}$) and rigidly rotating stars are about 0.180 and 0.207, respectively, with $R/M_g \sim 5$.[26] Hence, the rotating stars prepared here as initial conditions are not very compact and massive. We also note that for a rigidly rotating star at the mass-shedding limit (i.e., a rigidly rotating star of maximum rotational velocity), the ratio of the polar coordinate length to the equatorial coordinate length is $R_{\mathrm{ratio}} \simeq 0.57$ for $M_* = 0.05$ with $q \simeq 1.22$. For differentially rotating stars with $A = \varpi_e/3$ and ϖ_e, even a toroidal star of $R_{\mathrm{ratio}} = 0$ and $q \gg 1$ can be obtained. Since $R_{\mathrm{ratio}} \geq 0.65$ and $q < 1$, it is found that the rotation of stars here is not very rapid.

We note that T/W for differentially rotating stars is larger than that for rigidly rotating stars for an identical value of q. During collapse, T/W is expected to roughly increase in proportion to R^{-1} when J and M_g are approximately conserved. A star for which T/W is larger than the critical value (~ 0.25) will be unstable against the non-axisymmetric dynamical instability.[27] Thus, even if q and M_* are identical, a collapsing star of differentially rotating initial conditions is likely to be more susceptible to the non-axisymmetric instability than a rigidly rotating one.

To induce gravitational collapse, we initially reduce the pressure by changing K from $K_i = 1$ to a value less than unity without changing the profile of ρ_* and u_i. (Note that we recompute the constraint equations whenever we modify the initial equilibrium configurations.) In the case of the polytropic equations of state with

units for which $G = 1 = c$, $\bar{M}_* \equiv M_* K^{-n/2}$ is a non-dimensional quantity, and the maximum allowed value is 0.180 ($= \bar{M}_{*smax}$) for spherical stars and 0.207 for rigidly rotating stars, as mentioned above. Thus, if $K^{-1/2}$ is larger than about 0.18/0.05, a collapsing star of small q (i.e., $q \ll 1$) is likely to collapse to a black hole in the absence of shocks.[28] For rapidly rotating stars with $q = O(1)$, the criterion for $K^{-1/2}$ is expected to be larger by $O(1)$, due to effects of rotation, because for $q > 1$, no black hole would be formed.[6,8] In the presence of shocks, $K'(= P/\rho^\Gamma)$ increases at shocks, so that the threshold value of $K^{-1/2}$ for black hole formation is increased.

We should mention that we do not consider this numerical experiment to be realistic for description of stellar collapses in nature. In realistic stellar collapses, the equations of state are much more complicated, effects of cooling and heating due to microscopic processes are important, the initial stellar radius is much larger, and the initial density configuration and rotational profile may be much more complicated. In this paper, we focus on the dynamics of rotating collapse in general relativity, and pay particular attention to qualitative effects of rotation on the criterion for prompt collapse to black holes. We expect that the present study with its simple equations of states and initial conditions will be helpful for understanding qualitative features of realistic rotating stellar collapses.

§4. Numerical results

In numerical simulations, we basically adopt a fixed uniform grid in which $\Delta x = \Delta y = \Delta z =$ constant with grid size $(x, z) = (N + 1, N + 1)$. For collapse of rapidly rotating stars, the products after the collapses are often accompanied by very thin disks. To improve resolution in the direction perpendicular to the disk, we choose $\Delta x = \Delta y = 2\Delta z =$ constant using grid size $(N + 1, 2N + 1)$ in such cases. To check the convergence of our numerical results, we adopt different grid resolutions as $N = 180$, 270, 360 and 500. Typically, we choose $N = 360$ as the maximum grid number. Irrespective of the grid size, the grid covers the same computational domain, $0 \leq x, z \leq L$; namely, the resolution is improved by increasing N. We always prepare rotating stars whose surface at the equator ($\varpi = \varpi_e$) is located at $2L/3$ as initial conditions.

In numerical simulations, we have used the FACOM VX/4R machine in the data processing center of NAOJ. This is a vector-parallel machine composed of four vector processors, but we have used only one of four processors in the present numerical experiment. The typical memory and CPU time in one simulation with typical grid size $(361, 361)$ are about 400 MBytes and 25 hours for 15000 time steps. (We note that with help of parallelization, the CPU hours could be reduced, although we have not yet carried this out for the present numerical code.)

4.1. *Adiabatic collapse for rigidly rotating initial data*

Simulations of adiabatic collapses using polytropic equations of state and rigidly rotating initial data sets have been performed for models (B)–(G) described in Table I. For each set of initial conditions, the simulations were carried out changing the decrease factor of the pressure, K, over a wide range. In Fig. 1, we summa-
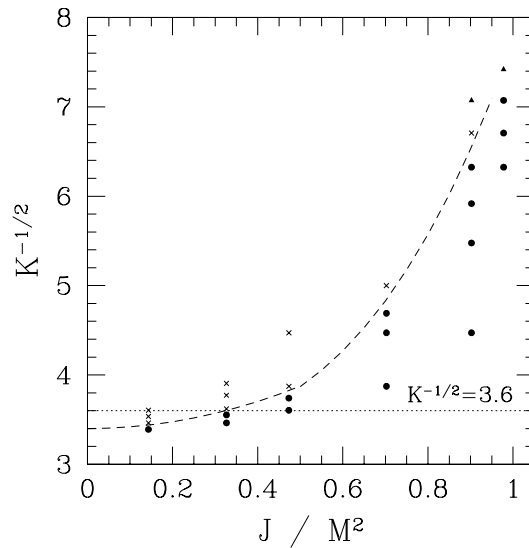
Fig. 1. Summary of the products in adiabatic collapse with rigidly rotating initial data. The horizontal and vertical axes denote $q = J/M_g^2$ and $K^{-1/2}$. The filled circles and crosses indicate that the products are a new compact star and a black hole, respectively. The filled triangles imply that we could not judge the nature of the products. The dotted line and dashed curves denote $K^{-1/2} = 18/5$ and the approximate threshold for black hole formation, respectively.

rize the products after collapse: The horizontal and vertical axes represent q and $K^{-1/2}$, respectively. The filled circles and crosses indicate that the products are a new star and a black hole, respectively. The filled triangles imply that we were not able to judge the nature of the products because a very thin disk is formed in the equatorial plane, which cannot be well resolved even with the maximum grid number.[29] (As for the process of the disk formation, see, e.g., the first four panels of Figs. 4 and 5.) The dotted line denotes $K^{-1/2} = 0.18/0.05$. The dashed curve denotes the approximate threshold which distinguishes between new star and black hole formation. In this numerical experiment, the threshold curve can be approximated by a quadratic function of q as $K^{-1/2} = 1.9q^2 + 3.4$ for $q < 0.5$, and it is a steeper function for larger q.

As we expected (see discussion above), the criterion for $K^{-1/2}$ for prompt collapse to black holes is ~ 3.6 for small q (i.e., $q < 0.5$). This implies that for $q < 0.5$, the effect of rotation is not very important for supporting the self-gravity of formed rotating stars. However, with increasing q, the critical value of $K^{-1/2}$ increases, and for $q \simeq 0.9$, it becomes ~ 6–6.5, which implies that a black hole is not formed after collapse even if $\bar{M}_* (= K^{-1/2}M_*)$ is $\sim 75\%$ larger than $\bar{M}_{*\mathrm{smax}}$. For model (B), the critical value of $K^{-1/2}$ can be ~ 7 or even larger; i.e., $\bar{M}_*$ of the resulting star can be twice as large as $\bar{M}_{*\mathrm{smax}}$. For this model, the maximum allowed value of $K^{-1/2}$ might be much larger, but it is difficult to perform accurate simulations for such a large decrease factor, because the thickness of the formed disk is too small to be well resolved.[29]
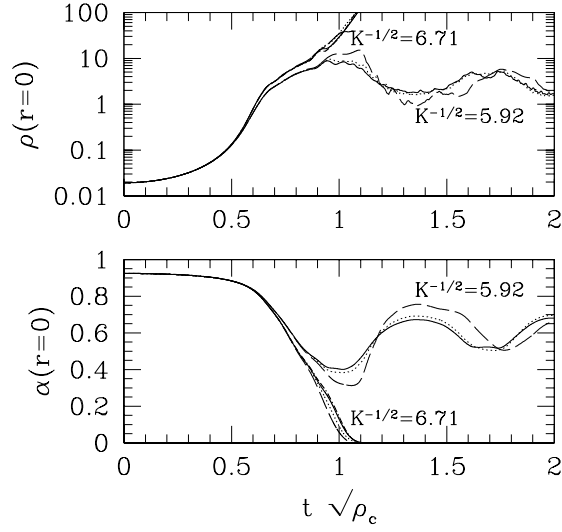
Fig. 2. Time evolution of ρ and α at $r = 0$ for model (C) with $K^{-1/2} = 5.92$ and 6.71. The solid, dotted, dashed, and dotted-dashed curves represent the results for $(361, 361)$, $(271, 271)$, $(181, 181)$ and $(361, 721)$ grid resolutions, respectively.
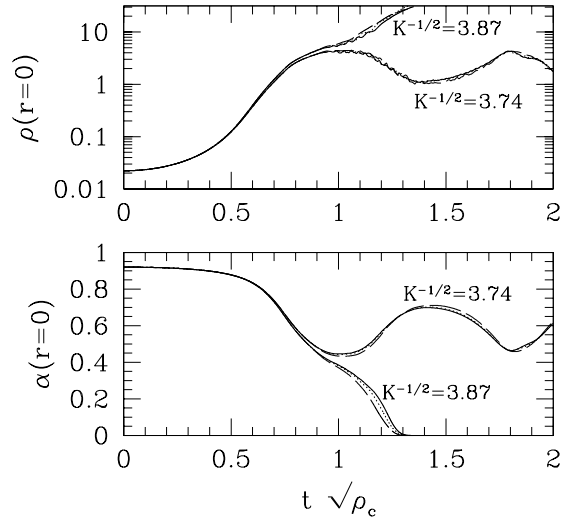

Fig. 3. The same as Fig. 2, but for model (E) with $K^{-1/2} = 3.74$ and 3.87.

In Figs. 2 and 3, we display the time evolution of the central density $\rho(r = 0)$ [30] and α at the origin for model (C) with $K^{-1/2} = 5.92$ and 6.71 and for model (E) with $K^{-1/2} = 3.74$ and 3.87. The results shown here are obtained with $(361, 361)$ (solid curves), $(271, 271)$ (dotted curves), $(181, 181)$ (dashed curves), and $(361, 721)$ (dotted-dashed curve). For model (C) with $K^{-1/2} = 5.92$ and model (E) with $K^{-1/2} = 3.87$, the collapse is halted during the evolution, resulting in an oscillating, compact star. On the other hand, for model (C) with $K^{-1/2} = 6.71$ and for model
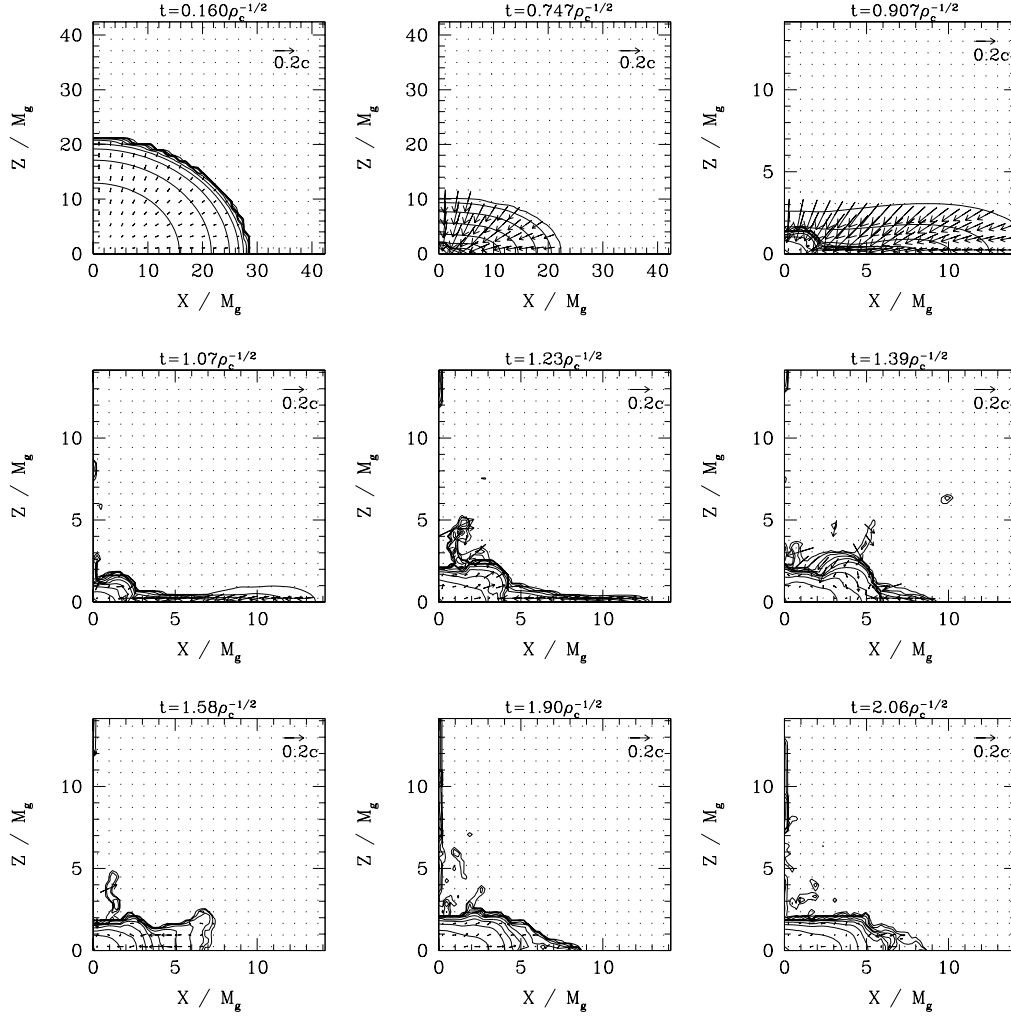
Fig. 4. Snapshots of density contours for ρ_* and the velocity flow for v^i in the (x, z) plane for model (C) with $K^{-1/2} = 5.92$. The contour lines are drawn for $\rho_*/\rho_{*\ max} = 10^{-0.4j}$ for $j = 0, 1, 2, \cdots, 10$, where $\rho_{*\ max}$ is 1.15, 422, 2054, 2705, 360, 264, 876, 315 and 244 times larger than $\rho_{*\ max}$ at $t = 0$ in each panel, respectively. The length of the velocity vector (the arrows) is normalized to $0.2c$. The time and length appear in units of $\rho_c^{-1/2}$ and GM_g/c^2 at $t = 0$, respectively.

(E) with $K^{-1/2} = 3.87$, the stars collapse to black holes in the dynamical time scale. As Figs. 2 and 3 show, these results depend only weakly on the resolution, implying that convergence is achieved fairly well.

In Figs. 4–7, we show snapshots of the contour lines and velocity fields in the x-z planes at selected time steps for model (C) with $K^{-1/2} = 5.92$ (Fig. 4) and 6.71 (Fig. 5), and for model (E) with $K^{-1/2} = 3.74$ (Fig. 6) and 3.87 (Fig. 7). All the results presented here were obtained with $(361, 361)$ grid resolution. For model (C) with larger initial decrease of the pressure, the rotating star collapses to a highly
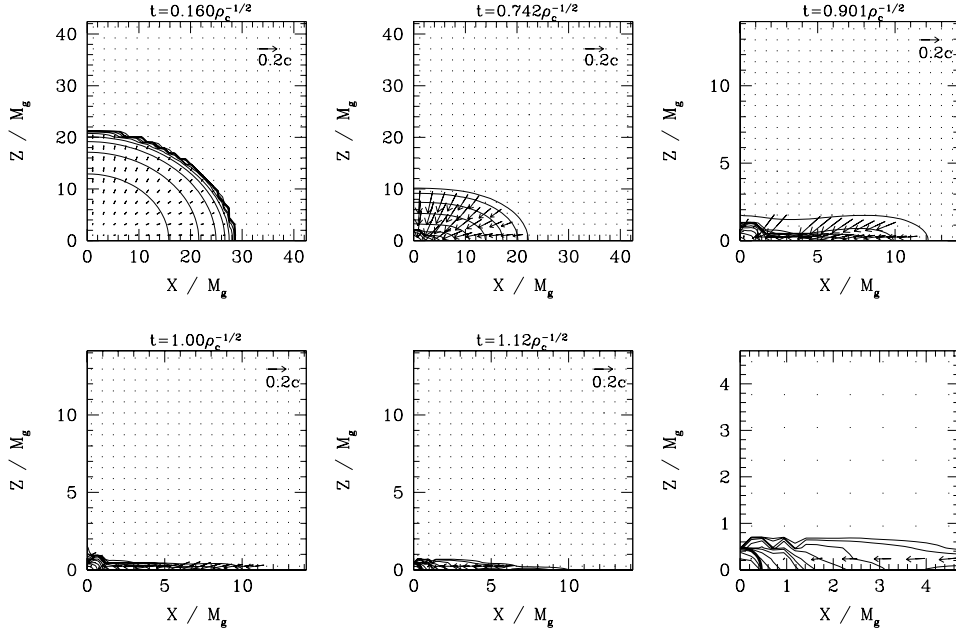
Fig. 5. The same as Fig. 4, but for model (C) with $K^{-1/2} = 6.71$. The contour lines are drawn
for $\rho_*/\rho_{* \ \mathrm{max}} = 10^{-0.4j}$ for $j = 0, 1, 2, \cdots, 10$, where $\rho_{* \ \mathrm{max}}$ is 1.15, 598, 7830, 6.37×10^4, and
3.89×10^5 times larger than $\rho_{* \ \mathrm{max}}$ at $t = 0$. The last panel is the magnification of the 5th
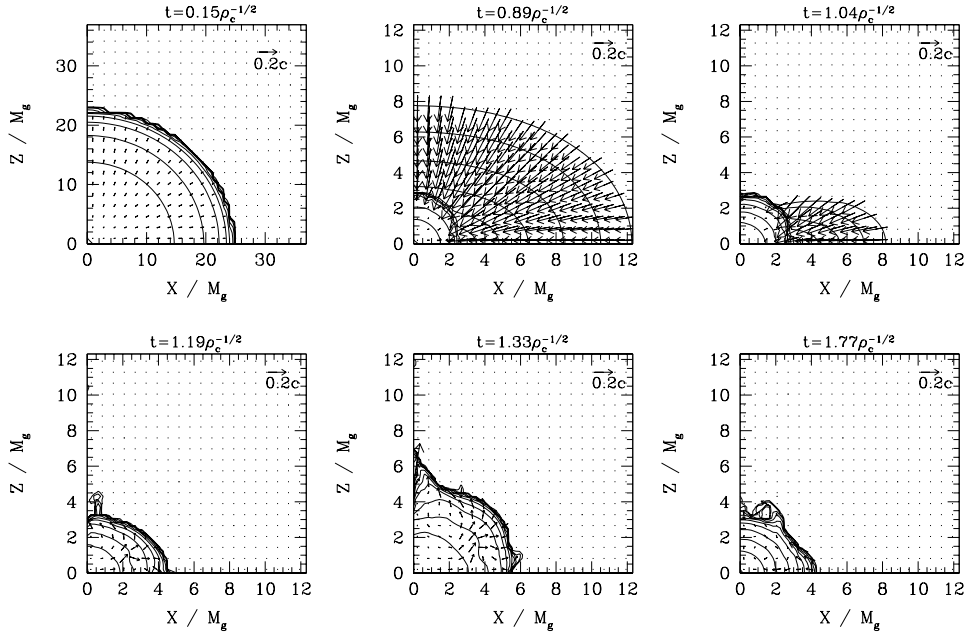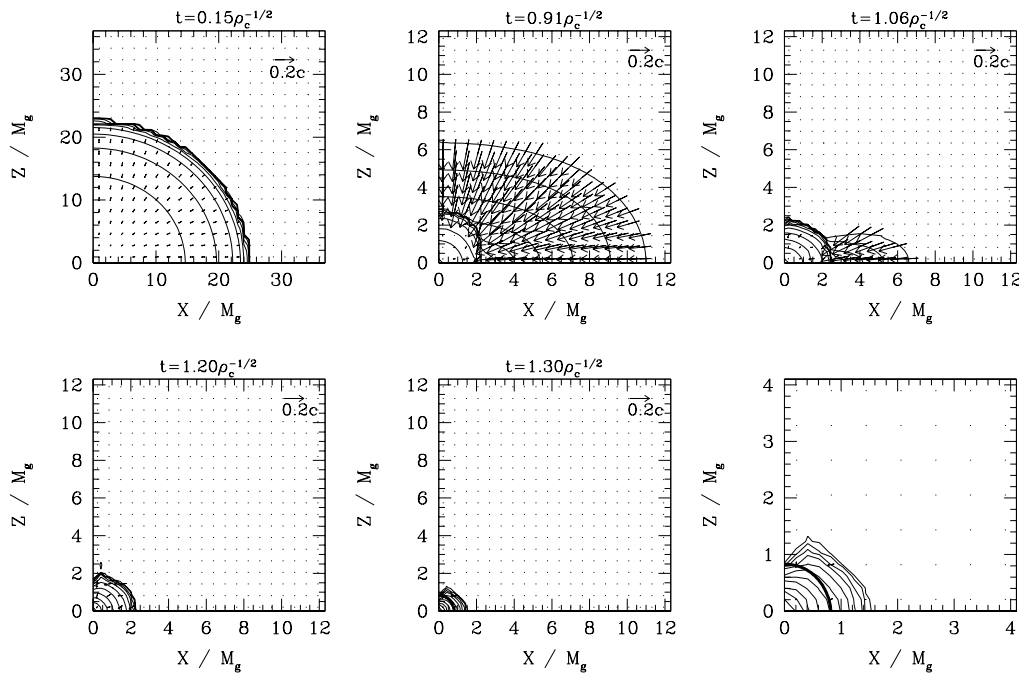panel. The thick solid curve in the last two panels indicates the apparent horizon.

Fig. 6. The same as Fig. 4, but for model (E) with $K^{-1/2} = 3.74$. The contour lines are drawn
for $\rho_*/\rho_{* \ \mathrm{max}} = 10^{-0.4j}$ for $j = 0, 1, 2, \cdots, 10$, where $\rho_{* \ \mathrm{max}}$ is 1.12, 724, 952, 475, 126 and 861
times larger than $\rho_{* \ \mathrm{max}}$ at $t = 0$.

Fig. 7. The same as Fig. 4, but for model (E) with $K^{-1/2} = 3.87$. The contour lines are drawn for $\rho_* / \rho_{*\ \max} = 10^{-0.4j}$ for $j = 0, 1, 2, \cdots, 10$, where $\rho_{*\ \max}$ is 1.23, 1120, 2670, 1.78×10^4, and 1.82×10^5 larger than the initial value. The last panel is the magnification of the 5th panel. The thick solid curve in the last two panels indicates the apparent horizon.

flattened object in the early stage. When the density increases sufficiently, the central region stops contracting, to form a core. On the other hand, the outer region, which forms a thin disk, is still collapsing. If the decrease factor of the pressure is not very large, the core subsequently expands, sweeping the surrounding disk, and finally an oscillating, oblate star is formed. On the other hand, for a sufficiently large decrease factor (i.e., $K^{-1/2} \gtrsim 6.5$), the core cannot expand, due to the insufficient pressure, resulting in a black hole after a fraction of matter accretion. In this case, the disk of a small fraction of mass appears to be formed around the black hole at $r \simeq 3$–$10 M_g$ (see also Fig. 9(a) and discussion below).

We note that even for model (C), the product is not a flattened object, but spheroidal one, if $K^{-1/2} \lesssim 4$. In such cases, the core radius is larger, and the evolution process is similar to that described by Fig. 6. The formation of a highly flattened object is a feature in the collapse for large q [i.e., $q = O(1)$] and for near critical values of $K^{-1/2}$ (i.e., $K^{-1/2} \gtrsim 6$), in other words, for the highly supramassive case in the sense $\bar{M}_* \gg \bar{M}_{*\mathrm{smax}}$.

For model (E), in which q is not very large, on the other hand, the collapse proceeds in a nearly spherical manner with tiny disks. When the density sufficiently increases, a nearly spherical core is formed. Since the decrease factor is smaller than that for model (C), the radius of the core is larger. For $K^{-1/2} = 3.74$, the core stops contracting, mainly due to the pressure force, subsequently forming an oscillating,
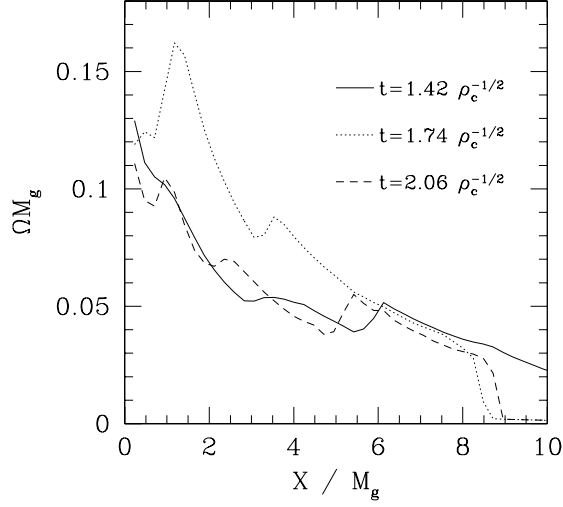
Fig. 8. Ω in units of M_g^{-1} at selected time steps for model (C) with $K^{-1/2} = 5.92$. Note that the rotating stars are oscillating with time, and at $t = 1.74\rho_c^{-1/2}$ the radius is smaller than at other times.

nearly spherical star. For a larger decrease factor, the collapse cannot be halted, and a black hole is finally formed, swallowing almost all the fluid elements.

The noteworthy difference between the evolution for models (C) and (E) for near critical values of K is with regard to the rest mass of the core in the early stage of its formation. For (C), the rest mass is not very large, because the fraction of the rest mass in the surrounding disk is fairly large (see the third panel of Fig. 4). This implies that the core does not have to support all of the rest mass of the system, and consequently the internal energy to support the self-gravity can be small. On the other hand, for (E), almost all the fluid elements accrete to the core simultaneously (see the third panel of Fig. 6), and the fraction of the rest mass which the core has to support is larger. This appears to be part of reason why the critical value of $K^{-1/2}$ for model (C) can be larger than that for model (E).

We should note that the product shown in Fig. 4 can have a large T/W, because according to a simple scaling law assuming the conservation of the angular momentum and the mass, we can expect it to roughly increase as $\sim (T/W)_i(R_i/R)$, where $(T/W)_i$ and R_i are T/W and R at $t = 0$. Since $T/W \sim 0.06$ at $t = 0$ (see Table I), T/W in a formed oscillating star would be ~ 0.2–0.3, and non-axisymmetric instabilities should be taken into account. A formed star is evidently *secularly* unstable with respect to gravitational wave emission to form a bar.[31] However, the secular time scale is much longer than the dynamical time scale, $\sim \rho_c^{-1/2}$, so that this would not be relevant even in a non-axisymmetric simulation performed only for $\sim 3\rho_c^{-1/2}$. A star also might be *dynamically* unstable to form a bar or spiral arms.[27] Using the results found in a previous paper,[27] we can roughly examine the dynamical stability. From Fig. 2, the normalized central density $\bar{\rho}(r = 0) \equiv K\rho(r = 0)$ is found to be between 0.05 and 0.15, while the normalized rest mass $\bar{M}_*$ is about 0.3. In Ref. 27),
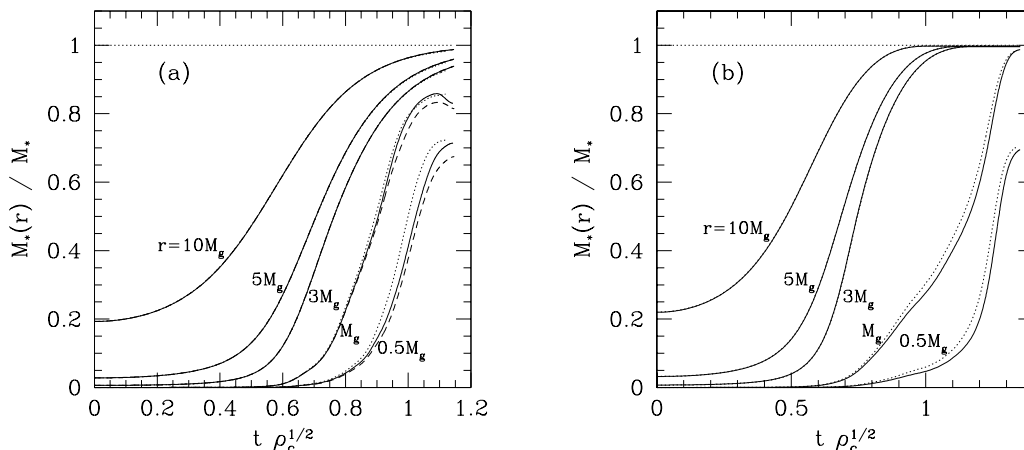
Fig. 9. Evolution of the fraction of the rest mass inside a coordinate radius r, $M_*(r)/M_*$ (a) for model (C) with $K^{-1/2} = 6.71$ and (b) for model (E) with $K^{-1/2} = 3.87$. The dotted, solid and dashed curves represent the results for $(271, 271)$, $(361, 361)$ and $(361, 721)$ grid resolutions, respectively.

we have found that if $\bar{\rho} \lesssim 0.1$, a star with $\bar{M}_* \gtrsim 0.3$ and $\Gamma = 2$ is dynamically unstable (cf. Fig. 2 of Ref. 27)). Thus, such a star is located near the threshold of the dynamical stability. Therefore, the process of the collapse might change if non-axisymmetric simulations were carried out.

In Fig. 8, we display the angular velocity Ω as a function of ϖ in the equatorial plane at selected times for model (C) with $K^{-1/2} = 5.92$. It is found that the star is differentially rotating, although it was rigidly rotating at $t = 0$. Since the formed star is not stationary but in an oscillating state, Ω varies with time and becomes a steeper function when the central density is large. As shown in a previous paper, [32] the effect of differential rotation can significantly increase the maximum allowed rest mass much beyond $\bar{M}_{*\text{smax}}$. This seems to be the reason why this highly supramassive object of rest mass much larger than $\bar{M}_{*\text{smax}}$ did not collapse to a black hole in this simulation.

We, however, note that the differential rotation will be changed to rigid rotation due to a magnetic field or viscosity, or that the angular momentum will be dissipated by the magnetic dipole radiation for a realistic neutron star formed after the collapse. [32] Thus, even if they are formed, any real supramassive stars of differential rotation will eventually collapse to black holes due to dissipation processes in the secular time scale.

In Figs. 9(a) and (b), we plot the fraction of the rest mass inside a coordinate radius r, $M_*(r)/M_*$, as a function of time (a) for model (C) with $K^{-1/2} = 6.71$ and (b) for model (E) with $K^{-1/2} = 3.87$. In both cases, black holes are formed on the dynamical time scale. Here, $M_*(r)$ is defined as

$$M_*(r) = 4\pi \int_{r' < r} x' dx' dz' \rho_*. \tag{4·1}$$

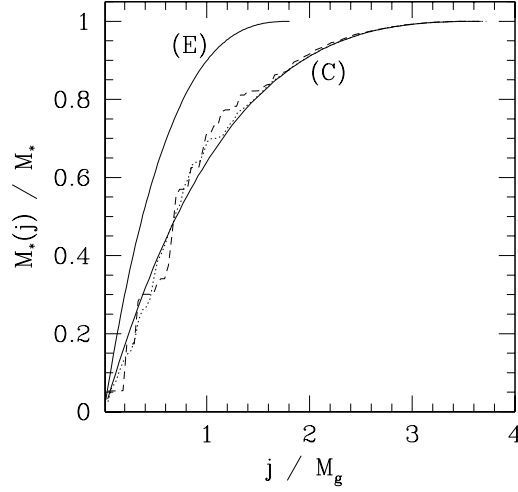The dotted, solid and dashed curves denote the results for $(271, 271)$, $(361, 361)$ and

Fig. 10. $M_*(j)/M_*$ as a function of j/M_g for models (C) and (E). The solid, dotted and dashed curves for model (C) denote the results at $t\rho_c^{1/2} = 0$, 0.901, and 1.10 for $K^{-1/2} = 6.71$.

$(361, 721)$ grid resolutions, respectively. As expected from Fig. 7, almost all the fluid elements are swallowed inside the apparent horizon located for $r \sim M_g$ for model (E). On the other hand, a small fraction of mass could form a disk around a black hole for model (C). Since the simulation crashed soon after the formation of the apparent horizon at $t \sim 1.15\rho^{-1/2}$, it is not possible to draw a definite conclusion from Fig. 9(a). However, Fig. 9(a) appears to suggest that $\sim 5\%$ of the total rest mass might form a disk around a black hole for $r \sim 3\text{--}10M_g$.[33] The reason for these results can be explained from the specific angular momentum distribution at $t = 0$ as follows.

In Fig. 10, we show $M_*(j)/M_*$ as a function of j/M_g for models (C) and (E) (note that M_g here denotes the initial value). For (C), we show it at selected time steps to demonstrate that the specific angular momentum spectrum $M_*(j)$ is preserved during the evolution fairly accurately. In both models, the specific angular momentum j is a monotonically increasing function of ϖ, and at the equator, it is $\sim 3.6M_g$ for model (C) and $\sim 1.8M_g$ for model (E). Taking into account that J is a conserved quantity, M_g is almost conserved, and the disk mass occupies only a small fraction of the total mass, we can expect that q of the formed black hole should be approximately equal to the initial value. Thus, the specific angular momentum at the innermost stable circular orbit in the equatorial plane around the formed Kerr black holes, which is the minimum allowed value for a test particle orbiting a Kerr black hole, is $\sim 2.1M_g$ for model (C) and $\sim 2.9M_g$ for (E).[34] It is immediately found that the specific angular momentum of no fluid elements is large enough to form a disk around the black hole for model (E). For model (C), a fraction of fluid elements of j between $\sim 2.1M_g$ and $3.6M_g$ can form a disk, but Fig. 10 shows that the mass fraction is only $\sim 6\%$, which is in approximate agreement with the fraction of the disk mass found in the numerical simulation.

4.2. *Adiabatic collapse for differentially rotating initial data*

Simulations of adiabatic collapses using polytropic equations of state and differentially rotating initial data sets have been performed for models (H)–(K) described in Table II and for models (L)–(O) in Table III. For each set of initial conditions, the simulations were carried out changing the decrease factor of the pressure for a
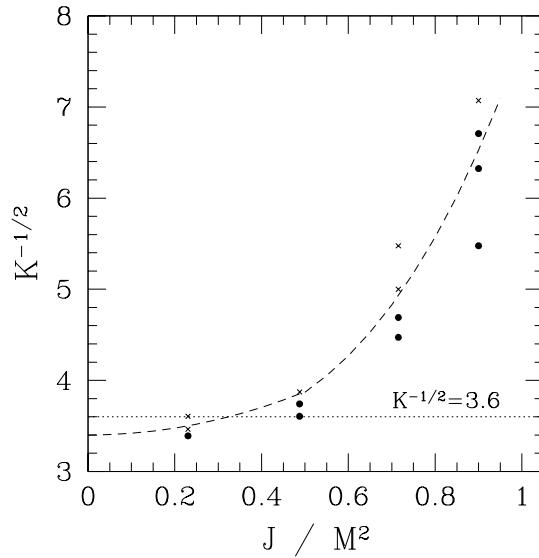

Fig. 11.   The same as Fig. 1, but for differentially rotating initial data with $A = \varpi_e/3$. The dashed curve represents the approximate threshold for black hole formation for rigidly rotating initial data.
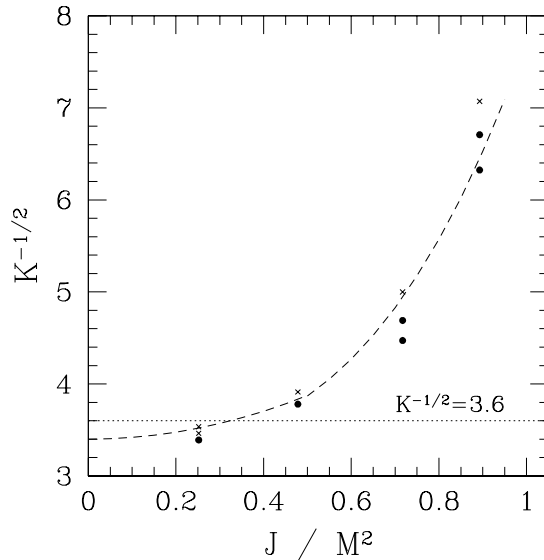
Fig. 12.   The same as Fig. 11, but for differentially rotating initial data with $A = \varpi_e$.

wide range. In Figs. 11 and 12, we summarize the products formed after collapse for $A = \varpi_e/3$ and $A = \varpi_e$ in the same manner as for Fig. 1. Note that the dashed curves denote the approximate threshold for black hole formation (i.e., below the dashed curves, a stable star is formed) for rigidly rotating initial data sets. It is found that the threshold for the differentially rotating initial conditions almost coincides with that for the rigidly rotating ones. Therefore, for the moderate range of rotational profiles we have investigated ($\varpi_e/3 \leq A \leq \infty$), the criterion of black hole formation depends only weakly on the initial rotational profile.

On the other hand, the products after the collapse depend strongly on the initial rotational profile, in particular, for $q \simeq 0.9$: For rigidly rotating initial data, the star remains a spheroid in the collapse even if $q \simeq 0.9$. On the other hand, it becomes a toroid for differentially rotating initial data with $A = \varpi_e/3$. To illustrate this fact, we display snapshots of the contour lines and velocity fields in the x-z planes at selected time steps for model (H) with $K^{-1/2} = 6.32$ in Fig. 13. In this case, the star does not form a black hole, but a toroid. As in the case of rigidly rotating initial data, fluid elements which are initially located far from $\varpi = 0$ collapse toward the central region in the early phase. On the other hand, those near the symmetric axis do not simply collapse toward the center, but slightly expand in the ϖ direction. This seems to be due to the effect of strong centrifugal force near the z axis (note that Ω at $\varpi = 0$ is initially about 4 times larger than that for the rigidly rotating cases of identical q). As a result of these types of motion, the collapsed object forms a ring-shape core in the early stage (cf. the third panel). The ring subsequently collapses toward the center, to become a very compact toroid (cf. the fifth and sixth panels). However, the centrifugal force and/or pressure hang up the collapse, and subsequently the ring expands with the formation of a jet along the symmetric axis (cf. the seventh panel). Once it reaches a maximum expansion at $t \sim 1.5\rho_{\max}^{-1/2}$, the ring begins to contract again to form a compact toroid (cf. the eighth panel), and this oscillating motion is repeated.

Here, we note that the maximum normalized density of the ring is very small, $\bar{\rho}_{\max} \sim 0.03$ at $t \sim 1.5\rho_{\max}^{-1/2}$, while $\bar{M}_*$ is very large, ~ 3.1. This implies that the ring would be dynamically unstable with respect to formation of a bar and/or spiral arms, or with respect to fission in a non-axisymmetric simulation. [27] This result is different from that in the case of rigidly rotating initial data, in which a collapsed object seems to be marginally stable, and it suggests that a collapsed object of differentially rotating initial data could be more susceptible to a non-axisymmetric, dynamical instability than that of rigidly rotating initial data, even if q is identical initially.

For model (H) with $K^{-1/2} > 7$, black holes are formed. For these cases, the evolution processes until $t \sim \rho_{\max}^{-1/2}$ are essentially the same as that shown in Fig. 13, but the star subsequently collapses, without bounce. In this black hole formation case, almost all the fluid elements are swallowed inside the black holes quickly. This can be understood from the sixth panel of Fig. 13. This result is in contrast to that in the black hole formation for model (C). The reason is as follows. In the case of a steep differentially rotational profile at $t = 0$, the specific angular momentum near
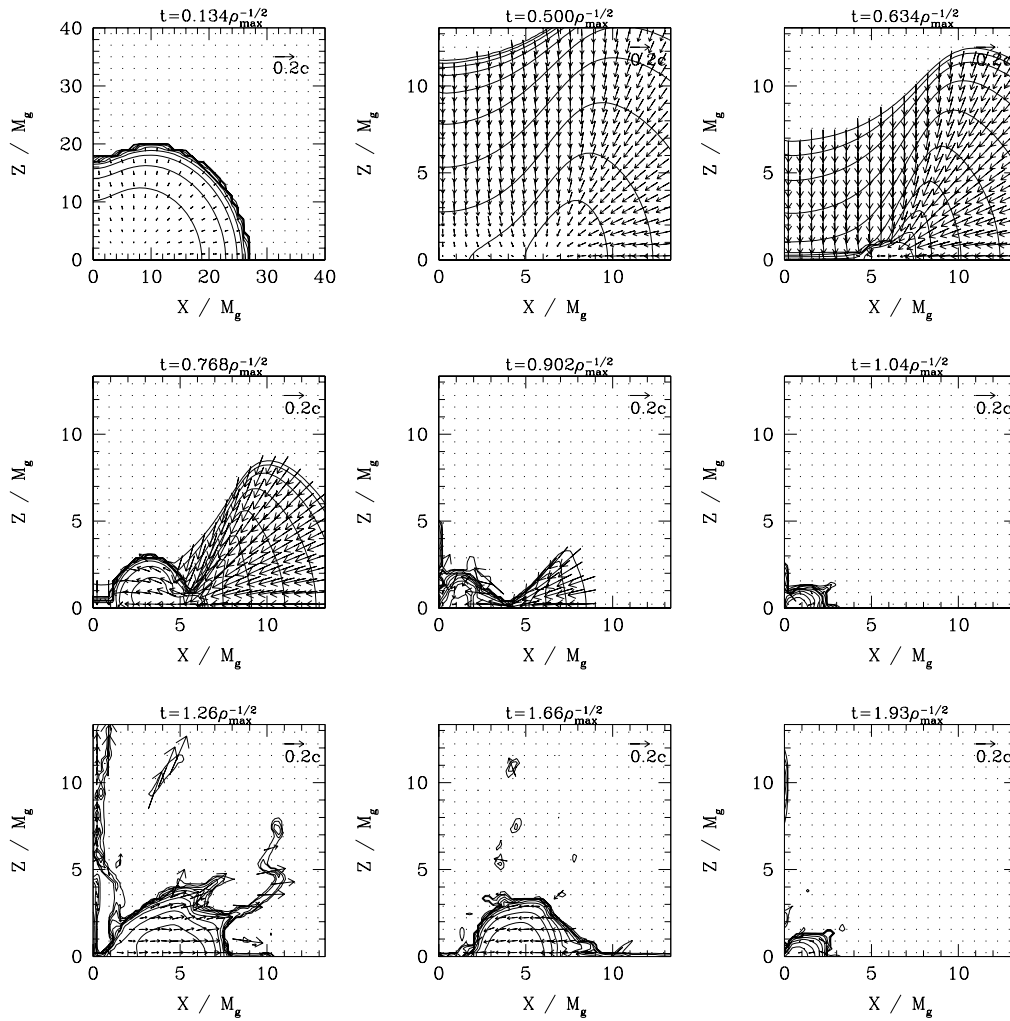
Fig. 13. The same as Fig. 4, but for model (H) with $K^{-1/2} = 6.32$. The contour lines are drawn for $\rho_* / \rho_{*\ \max} = 10^{-0.4j}$ for $j = 0, 1, 2, \cdots, 10$, where $\rho_{*\ \max}$ is 1.10, 9.22, 77.7, 99.3, 1781, 4131, 75.1, 85.3, and 3619 times larger than $\rho_{*\ \max}$ at $t = 0$. The time appears in units of $\rho_{\max}^{-1/2}$ at $t = 0$.

the equator is much smaller than that for rigidly rotating cases. For model (H), the specific angular momentum at the equator is $0.94 M_g$, which is smaller than the value at the innermost stable circular orbit of a Kerr black hole with $q = 0.9$ and mass M_g. Consequently, it is unlikely for a disk to be formed. We argue this point in §5 in detail.

In Fig. 14, we show snapshots of the contour lines and velocity fields in the x-z plane at selected time steps for model (J) with $K^{-1/2} = 3.74$, in which a black hole is not formed. Since q is not very large (~ 0.48) in this case, a ring is not formed throughout the entire evolution. However, the effect of the rotation appears to be significant. Compared with the core formed in the simulation of model (E),
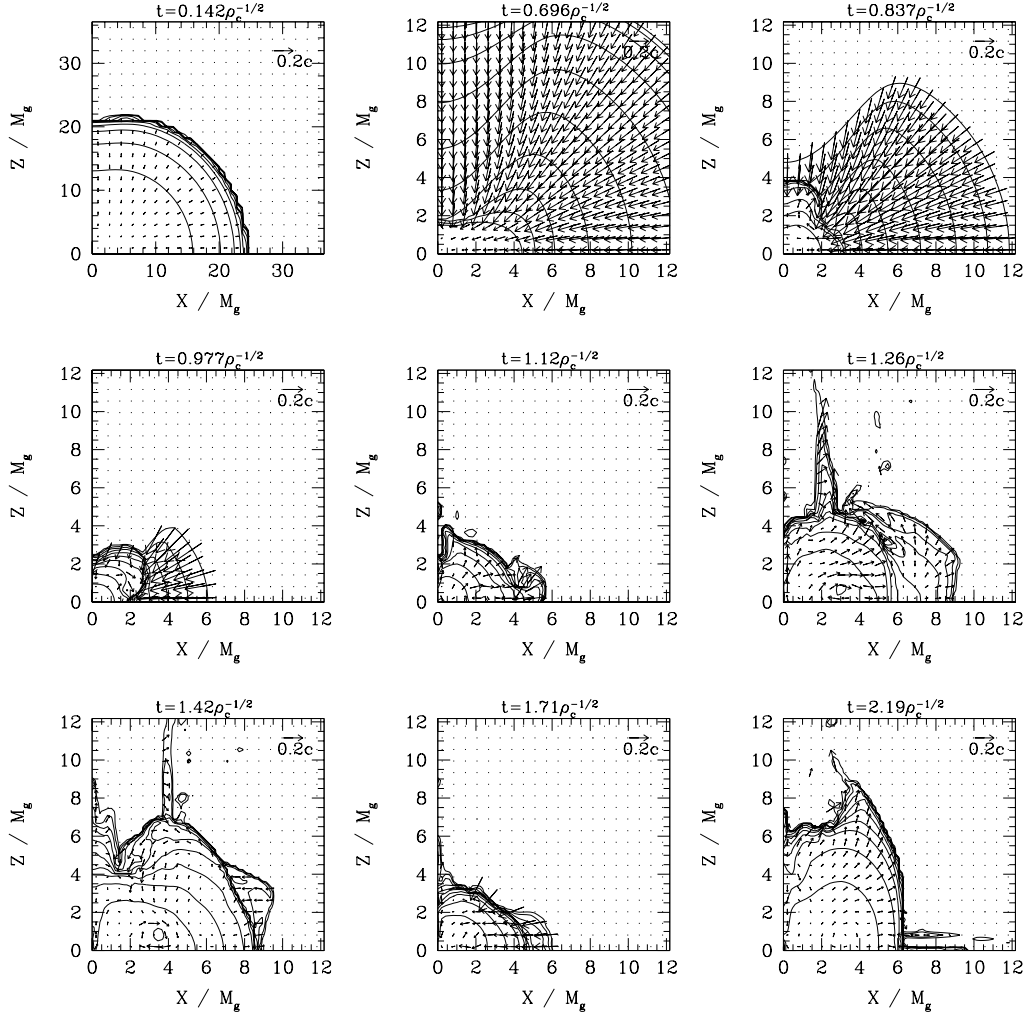
Fig. 14. The same as Fig. 13, but for model (J) with $K^{-1/2} = 3.74$. The contour lines are drawn for $\rho_*/\rho_{* \ max} = 10^{-0.4j}$ for $j = 0, 1, 2, \cdots, 10$, where $\rho_{* \ max}$ is 1.06, 61.5, 436, 1554, 610, 63.7, 41.8, 241, and 36.5 times larger than $\rho_{* \ max}$ at $t = 0$. Note that $\rho_c = \rho_{max}$ at $t = 0$ in this case.

in which q is nearly equal to that for model (J), the shape of the core is much more deformed, due to the effect of the differential rotation initially given (compare the second panel with the second panel in Fig. 6). Also, a violent non-spherical oscillation is found after formation of the new star. These results imply that even if q and M_* are identical initially, the shape and motion of the products after collapse depend strongly on the initial rotational profiles.

4.3. *Non-adiabatic case*

Simulations of non-adiabatic collapses using a Γ-law equation of state have been performed for models (C)–(E) and (H)–(J) described in Tables I and II. In Figs. 15 and 16, we summarize the products after collapses for (C)–(E) and (H)–(J) in the
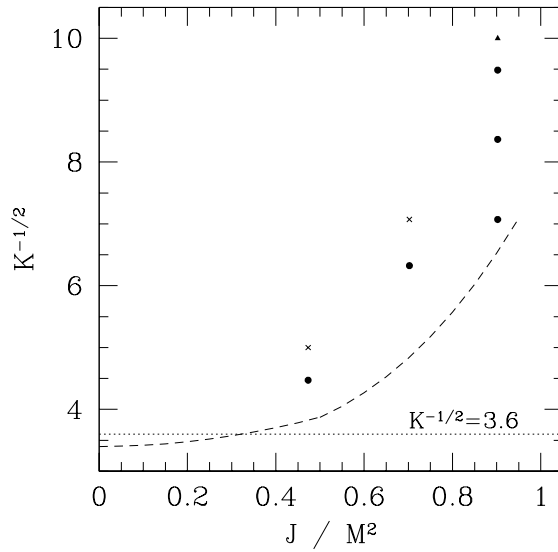
Fig. 15.   The same as Fig. 1, but for non-adiabatic collapse with rigidly rotating initial data. The dashed curve represents the approximate threshold for black hole formation in adiabatic collapse.
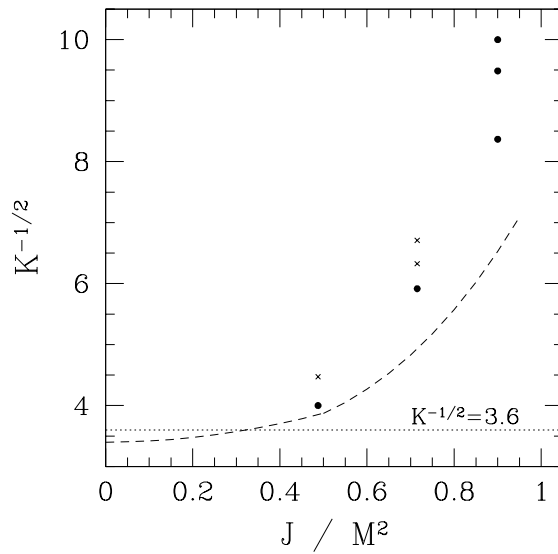

Fig. 16.   The same as Fig. 1, but for non-adiabatic collapse for differentially rotating initial data with $A = \varpi_e/3$. The dashed curve represents the approximate threshold for black hole formation in adiabatic collapse.

same manner as for Fig. 1. The dashed curve denotes the approximate threshold for black hole formation in the adiabatic collapses. Obviously, the shock heating raises the criterion for $K^{-1/2}$ for prompt formation of black holes. It is found that the effect is in particular significant for larger q. We note that for model (C), we cannot judge the nature of the product for $K^{-1/2} \geq 10$, because a very thin disk is
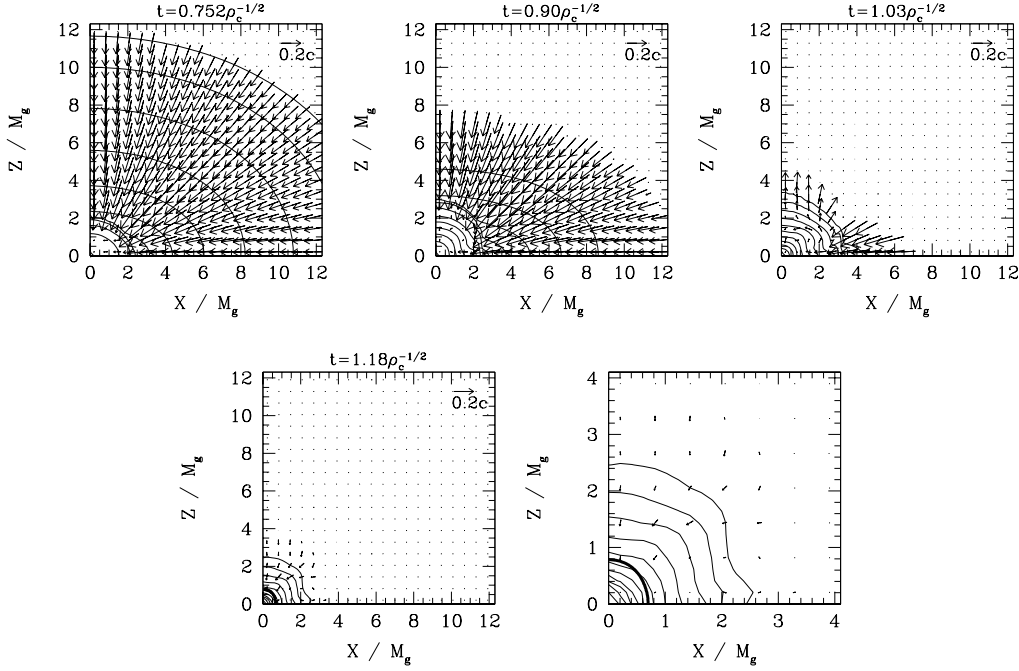
Fig. 17. The same as Fig. 4, but for non-adiabatic collapse for model (E) with $K^{-1/2} = 5.00$. The
contour lines are drawn for $\rho_*/\rho_{*\,\text{max}} = 10^{-0.4j}$ for $j = 0, 1, 2, \cdots, 10$, where $\rho_{*\,\text{max}}$ is 643, 3814,
2.65×10^4, and 2.26×10^5 times larger than $\rho_{*\,\text{max}}$ at $t = 0$. The last panel is the magnification
of the 4th panel. The thick solid curve in the last two panels indicates the apparent horizon.

formed in the equatorial plane and cannot be well resolved even with $(501, 501)$ grid
resolution. For model (H), formation of black holes is not found for $K^{-1/2} \leq 10$.
For larger $K^{-1/2}$ (i.e., $K^{-1/2} \gg 10$), black holes would be formed for both models,
but to find this formation, simulations with finer resolution are necessary to resolve
the thin disk and/or thin ring.

Even in the presence of the shock heating, the formation process of black holes
is not modified drastically. In Fig. 17, we show snapshots of the contour lines and
velocity fields in the x-z planes at selected time steps for model (E) with $K^{-1/2} =$
5.00 as an example. Although shocks are generated at the formation of the central
core (cf. the second panel), they stall due to the subsequent accretion of matter, and
hence the collapse is never halted, resulting in a black hole on the dynamical time
scale.

On the other hand, the process in the case of no black hole formation is con-
siderably affected by shocks, in particular, for $q \sim 0.9$. In Figs. 18–21, we show
snapshots of the contour lines and velocity fields in the x-z planes at selected time
steps for model (C) with $K^{-1/2} = 8.37$, for model (E) with $K^{-1/2} = 4.47$, for model
(H) with $K^{-1/2} = 9.49$, and for model (J) with $K^{-1/2} = 4.00$.

In the case of small q, spheroidal shocks are formed around the surface of the
central core (cf. the first panel in Figs. 19 and 21). This implies that the shock
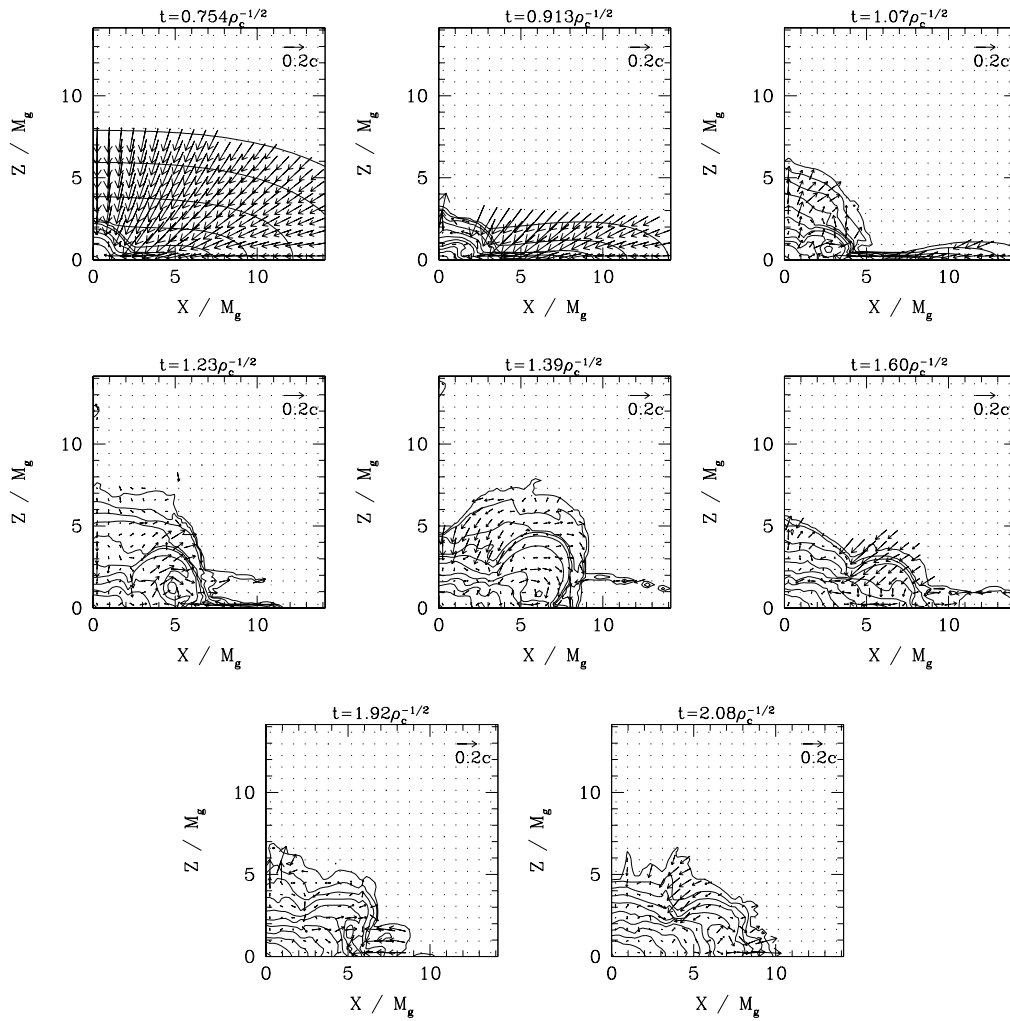heating is effective only around the spheroidal shell. Indeed, $K'(x^\mu)$ around the

Fig. 18. The same as Fig. 4, but for non-adiabatic collapse for model (C) with $K^{-1/2} = 8.37$. The contour lines are drawn for $\rho_*/\rho_{* \ max} = 10^{-0.4j}$ for $j = 0, 1, 2, \cdots, 10$, where $\rho_{* \ max}$ is 1178, 5015, 1186, 403, 317, 619, 814, and 436 times larger than $\rho_{* \ max}$ at $t = 0$.

center of the core remains nearly constant throughout the evolution. Therefore, the shock heating is not very effective for increase of the internal energy in the high density region. Instead, the energy generated by shocks at the shell is effectively used to provide the energy to the surrounding matter, which subsequently expands outward.

On the other hand, the formation mechanism of shocks for $q \simeq 0.9$ and $K^{-1/2}M_*$ $\gg \bar{M}_{*smax}$ is completely different from that for smaller q (see Figs. 18 and 20): In the very early phase, the shocks around the small spheroidal core (for model (C)) or disk-plus-ring (for model (H)) are formed. Here, the shape of the shocks depends strongly on the rotational profile initially given. The reason why the mass fraction around the shock forming, high density region is small is that a large fraction of mass, which
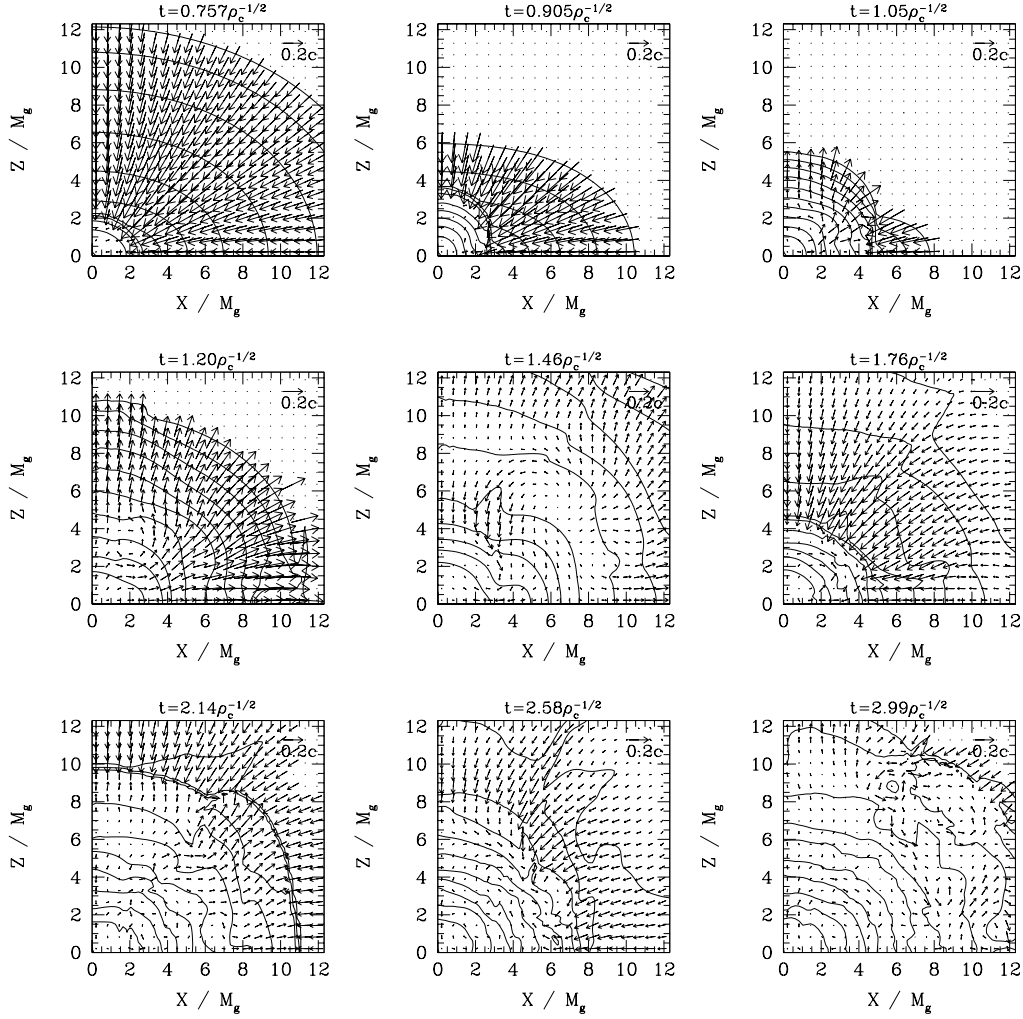
Fig. 19. The same as Fig. 4, but for non-adiabatic collapse for model (E) with $K^{-1/2} = 4.47$. The contour lines are drawn for $\rho_*/\rho_{* \, max} = 10^{-0.4j}$ for $j = 0, 1, 2, \cdots, 10$, where $\rho_{* \, max}$ is 424, 1566, 1027, 151, 100, 360, 162, 289, and 187 times larger than $\rho_{* \, max}$ at $t = 0$.

is initially located at large ϖ, has not yet accreted, due to the centrifugal force, and the collapse proceeds mainly in the z direction. Since the mass of the high density region is small, prompt formation of a black hole does not occur in spite of the small internal energy.

   The shocks formed in the early phase subsequently expand in the z direction for model (C) and toward the z axis for model (H), because a large amount of matter still accretes near the equatorial plane and prevents the shocks from expanding outward. The mass fraction near the symmetric axis is not very large, so that this shock expansion is not efficiently used for sweeping the accreting matter around the cores. The evolution processes after a substantial fraction of matter residing in the outer part has accreted to the small cores are different for the two cases. For model (C),
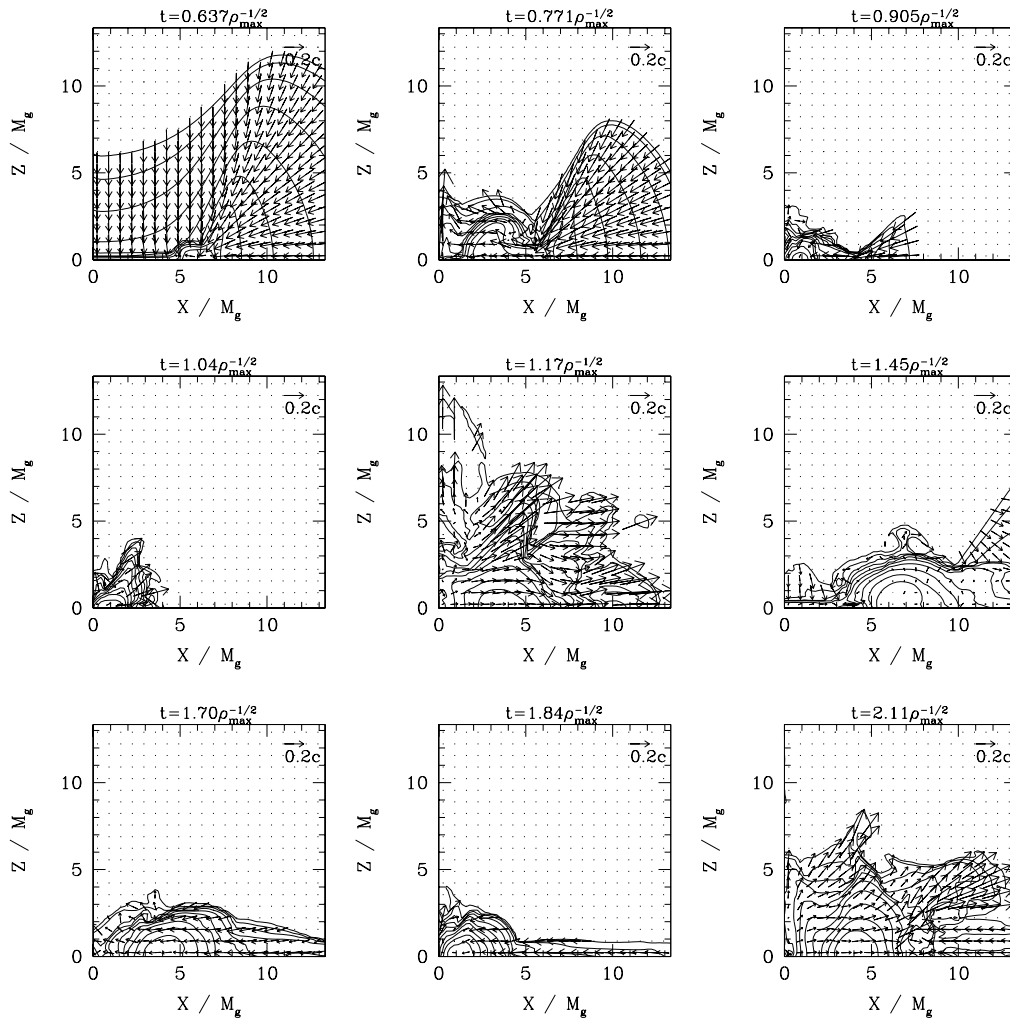
Fig. 20. The same as Fig. 4, but for non-adiabatic collapse for model (H) with $K^{-1/2} = 9.49$. The contour lines are drawn for $\rho_*/\rho_{* \ max} = 10^{-0.4j}$ for $j = 0, 1, 2, \cdots, 10$, where $\rho_{* \ max}$ is 165, 168, 4276, 2684, 165, 73.6, 161, 1136, 1192, and 124 times larger than $\rho_{* \ max}$ at $t = 0$. The time appears in units of $\rho_{max}^{-1/2}$ at $t = 0$.

the shocks formed in the interface between the small core and the surrounding disk initiate expansion that sweeps the matter (cf. the fourth and fifth panels in Fig. 18). However, the expansion is not very powerful because a part of the internal energy has already been used in the first expansion in the z direction and these second shocks are not very strong. For model (H), the evolution process is more complicated. During the accretion of the matter from the outer part to the core, the toroidal core starts contracting toward the z axis without significant shock formation (cf. the third panel in Fig. 20); i.e., in this case, shocks which sweep accreting matter are not formed. Then, the inner surface of the toroid collides at the z axis (cf. the fourth panel), and as a result, a shock is formed along the z axis. This shock subsequently
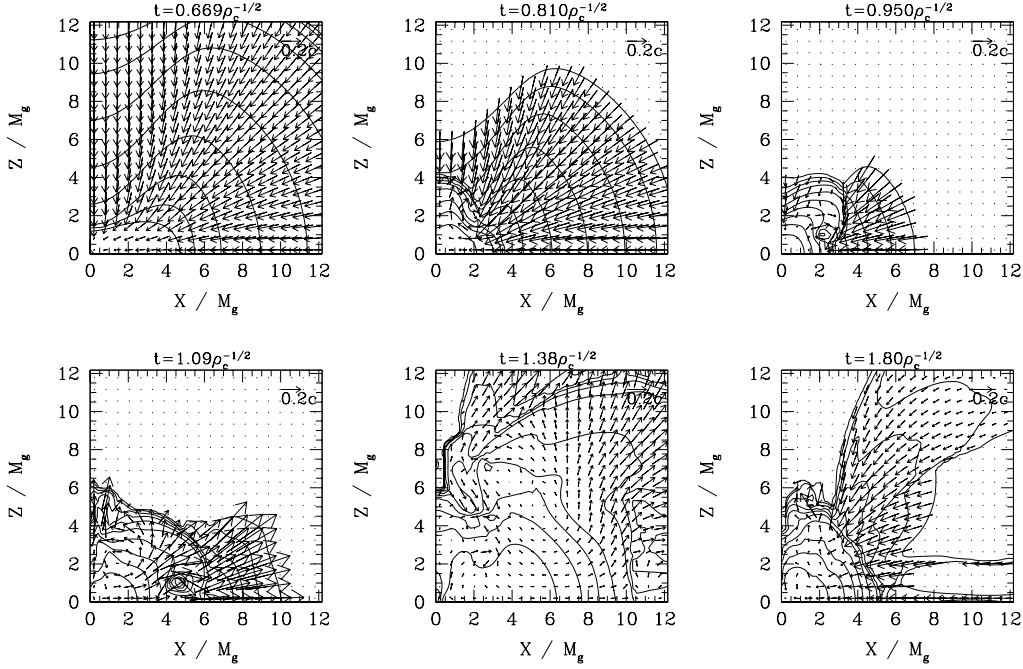
Fig. 21.   The same as Fig. 4, but for non-adiabatic collapse for model (K) with $K^{-1/2} = 4.00$. The contour lines are drawn for $\rho_*/\rho_{*\,max} = 10^{-0.4j}$ for $j = 0, 1, 2, \cdots, 10$, where $\rho_{*\,max}$ is 45.9, 379, 1366, 256, 23.1, and 219 times larger than $\rho_{*\,max}$ at $t = 0$. Note that $\rho_c = \rho_{max}$ at $t = 0$ in this case.

expands mainly in the ϖ direction (cf. the fifth panel), contributing to an increase of the internal energy for a large fraction of mass elements in the toroid. The toroid oscillates nearly periodically, so that this process is repeated (cf. the sixth–ninth panels). For both models (C) and (H), several different types of shocks are formed in different stages incoherently. Consequently, the motion of the shocks is less coherent and less efficient in sweeping the accreting matter than for the small q case. This result appears to represent an extreme example in which rapid rotation prevents the formation of coherent shocks. [35)

The above described mechanism of shock formation also explains the reason that the threshold value of $K^{-1/2}$ is much larger than that in the absence of shocks only for the large q case. For small q, shocks are generated near the surface of a central dense core, so that the entropy can be increased only in the surface region of low density. Consequently, the shock heating is not very effective for increasing the internal energy of the central core. On the other hand, for large q with large pressure decrease (i.e., $K^{-1/2}M_* \gg \bar{M}_{*\mathrm{smax}}$), shocks can be generated near high density regions, i.e., around the small cores and the disks. Indeed, K' is increased by a large factor for most fluid elements. This is due to the highly non-spherical motion induced by the large centrifugal force, as mentioned above. As a result, a large amount of the matter is affected by the shock heating, resulting in a large increase of the total internal energy. Thus, although rapid rotation prevents the

formation of coherent shocks, it could contribute to a shock heating that is efficient for preventing prompt collapse to black holes.

§5. Summary and discussion

We constructed a new numerical code for axisymmetric hydrodynamic simulations in full general relativity. In this code, the Einstein field equation is solved using Cartesian coordinates with appropriate boundary conditions, while the hydrodynamic equations are solved in cylindrical coordinates. It was shown from numerical experiments that this method is sufficiently robust to perform stable and well-resolved computations for rotating stellar collapse.

Using this code, we have investigated the criterion for black hole formation after rotating stellar collapses. It is found that the effect of rotation could play an important role in preventing prompt formation of black holes. For the case in which the angular momentum parameter q is smaller than ~ 0.5, a black hole is formed if the total rest mass is slightly larger than the maximum allowed rest mass of spherical stars ($\bar{M}_{*\mathrm{smax}}$), implying that the effect of rotation is not very important. On the other hand, the threshold of the total rest mass can be significantly increased by the effect of rotation for $q \lesssim 1$: e.g., for $q \sim 0.9$, the threshold value is about 70–80% larger than $\bar{M}_{*\mathrm{smax}}$. The self-gravity of such large mass products is supported by rapid, differential rotation. These results are found to depend only weakly on the initial rotational profile within the range that we have investigated.

We have found that the formation mechanism of shocks depends strongly on the rotational parameter q. For collapse of slowly rotating stars of $q < 0.5$, shocks are formed at the spheroidal shell around a high density core. As a result, shock heating is effective only around the shell and is not very helpful for increasing the internal energy of the central core. On the other hand, shocks can be formed in a highly non-spherical manner and near the high density region in the collapse of rapidly rotating, supramassive stars for which $q = O(1)$ and $K^{-1/2}M_* \gg \bar{M}_{*\mathrm{smax}}$. Since the centrifugal force is large in this case, a large amount of matter at large ϖ cannot accrete immediately, and the high density regions formed in the early stage could have highly non-spherical shapes. As a result, shocks can be formed in a highly non-spherical manner around the high density region. (The shapes of the shocks depend strongly on the initial rotational profile.) Because of the matter accretion around the equatorial plane, shocks cannot expand coherently, and hence they cannot sweep the accreting matter effectively. However, shocks can contribute to the heating for a large number of the mass elements, because they are formed near the high density regions. Consequently, they prevent prompt collapse to black holes even for highly supramassive stars with $K^{-1/2}M_* \gg \bar{M}_{*\mathrm{smax}}$.

The numerical results reported in this paper indicate that the disk mass around formed black holes is not very large even for $q \simeq 0.9$. In a different setting, with different equations of state, different initial radii, and different initial rotational profiles, results could be modified. It is an interesting issue to clarify what kind of initial conditions are preferable for obtaining a system of a black hole surrounded by massive disks, because the formation of disks around a black hole [12] could play

an important role in nature. Here, we carry out a simple analysis to address that equations of state and initial velocity profiles of a star before collapse play a crucial role in determining the disk mass.

In the following, we assume that (1) rotating stars at $t = 0$ are not very compact, (2) black holes are formed only for $q < 1$, and (3) the fraction of the disk mass is much smaller than the total mass and that the value of q of a formed black hole is nearly equal to the initial value. Due to the assumption (1), the angular momentum can be approximately computed from initial data as

$$J \simeq \int dV \rho_* \varpi^2 \Omega, \tag{5·1}$$

where we use $h \simeq 1$ and $j \simeq \varpi^2 \Omega$. For simplicity, here, we consider Ω to be of the same form as in Eq. (3·2). For the case that $A \ll \varpi_e$, $J \simeq M_* A^2 \Omega_0 \simeq M_* \varpi_e^2 \Omega_e$, where Ω_e is the angular velocity at $\varpi = \varpi_e$. Then, q can be approximately written as $\varpi_e^2 \Omega_e / M_g$, where we use $M_g \simeq M_*$, due to the assumption (1). For the case $A \gg \varpi_e$, on the other hand, the star is in a state of nearly rigid rotation ($\Omega_0 = \Omega_e$), and $J = M_* \langle \varpi^2 \rangle \Omega_e$, where

$$\langle \varpi^2 \rangle \equiv \frac{1}{M_*} \int \rho_* \varpi^2 dV. \tag{5·2}$$

Consequently, $q \simeq \langle \varpi^2 \rangle \Omega_e / M_g$. Then, the specific angular momentum j can be approximately written as

$$j(\varpi) \simeq \varpi^2 \Omega_e \simeq \begin{cases} M_g q & \text{for } A \ll \varpi_e, \\ M_g q \varpi^2 / \langle \varpi^2 \rangle & \text{for } A \gg \varpi_e. \end{cases} \tag{5·3}$$

Thus, $j(\varpi)/M_g = q$ for $A \ll \varpi_e$, and $j(\varpi)/M_g \le q \varpi_e^2 / \langle \varpi^2 \rangle$ for $A \gg \varpi_e$. To form a disk around a black hole, j/M_g has to be larger than ℓ_{ISCO}, where ℓ_{ISCO} denotes j/M_g at the innermost circular orbit around a black hole which depends on q. ($\ell_{\text{ISCO}} = 1$ for $q = 1$, $\simeq 2.1$ for $q = 0.9$, and $\simeq 2\sqrt{3}$ for $q \ll 1$.) This implies that for $A \ll \varpi_e$, a disk cannot be formed, irrespective of the value of q for $q < 1$. For a star which was initially in rigid rotation, a disk can be formed if $q \varpi_e^2 / \langle \varpi^2 \rangle = O(1)$. For equilibrium stars with stiff equations of state, the density profile is not very centrally peaked, so that $\varpi_e^2 / \langle \varpi^2 \rangle$ is of $O(1)$. This implies that q has to be of $O(1)$ for disk formation. We presented such an example in §4.1. On the other hand, q may be smaller for equilibrium stars of soft equations of state for which the density profile is centrally peaked, and $\varpi_e^2 / \langle \varpi^2 \rangle$ can be much larger than unity. We note that $\varpi_e^2 / \langle \varpi^2 \rangle$ depends weakly on ϖ_e for non-relativistic stars of an identical equation of state. Thus, this conclusion is almost independent of the initial stellar radius. From these arguments, we can recognize that to obtain disks around a black hole, irrespective of the initial stellar radius, (i) stars before collapse should not have a steep differential rotational profile, but rather a nearly rigidly rotational profile, (ii) the value of q of stars before collapse should be of $O(1)$ if the equation of state is stiff, or stars before collapse should have a soft equation of state if $q \ll 1$. In realistic situations, a progenitor of a supernova just before collapse has a soft equation of state with $\Gamma \simeq 1.3$. Thus, a disk would be formed as long as the initial rotational profile is not too steep.

Although these conclusions would be qualitatively correct, nothing quantitative can be clarified at this time. In particular, we assumed that the disk mass is much smaller than the black hole mass in this analysis, but this might be incorrect for the case of soft equations of state. This is because the star is centrally condensed in this case, and it may be the case that only the central region collapses to form a black hole of a small mass fraction. Thus, to compute the disk mass in rotating stellar collapse correctly, numerical simulations are obviously necessary.

In this paper, we have studied rotating stellar collapse using simple equations of state and simple initial conditions which are not very realistic. We believe that the significant effects of rotation found here are qualitatively correct, but they might not be quantitatively realistic. To obtain a result applicable to realistic systems, we have to perform simulations using more realistic equations of state and initial conditions. We plan to perform such simulations in the future.

Acknowledgements

References

1) T. Nakamura, K. Oohara and Y. Kojima, Prog. Theor. Phys. Suppl. No. 90 (1987), 1.
2) R. Penrose, Nuovo Cim. **1** (1969), 252.
3) W. Israel, Phys. Rev. **164** (1967), 1776.
4) B. Carter, Phys. Rev. Lett. **34** (1971), 331.
5) For review of the uniqueness theorem, see, e.g., R. M. Wald, *General Relativity* (The University of Chicago Press, 1984), chapter 12.
6) T. Nakamura, Prog. Theor. Phys. **65** (1981), 1876; **70** (1983), 1144.
7) K. Maeda, M. Sasaki, T. Nakamura and S. Miyama, Prog. Theor. Phys. **63** (1980), 719.
8) R. F. Stark and T. Piran, Phys. Lett. **55** (1985), 891; in *Dynamical Spacetimes and Numerical Relativity*, ed. J. M. Centrella (Cambridge University Press), p. 40.
9) J. M. Bardeen and T. Piran, Phys. Rep. **96** (1983), 205.
10) Note, however, that collapse of a rotating cluster of collisionless matter is studied in the following reference: A. M. Abrahams, G. B. Cook, S. L. Shapiro and S. A. Teukolsky, Phys. Rev. **D49** (1994), 5153.
11) L. S. Finn and C. R. Evans, Astrophys. J. **351** (1990), 588.
    R. Mönchmeyer, G. Schäfer, E. Müller and R. Kates, Astron. Astrophys. **246** (1991), 417.
    S. Bonazzola and J.-A. Marck, Astron. Astrophys. **267** (1993), 623.
    S. Yamada and K. Sato, Astrophys. J. **450** (1995), 245.
    T. Zwerger and E. Müller, Astron. Astrophys. **332** (1997), 209.
    M. Rampp, E. Müller and M. Ruffert, Astron. Astrophys. **332** (1998), 969.
12) S. E. Woosley, Astrophys. J. **405** (1993), 273.
    B. Paczynski, Astrophys. J. **494** (1998), L45.
    A. I. MacFadyen and S. E. Woosley, Astrophys. J. **524** (1999), 262.
13) T. W. Baumgarte and S. L. Shapiro, Astrophys. J. **526** (1999), 941.
14) M. Shibata, Phys. Rev. **D60** (1999), 104052.
15) M. Shibata and K. Uryu, Phys. Rev. **D61** (2000), 064001.

16) But, for a special class of gauge conditions with appropriate prescriptions, it is still possible to preserve the accuracy and stability without artificial viscosity (e.g., D. Garfinkle, personal communication).

17) M. Alcubierre, S. Brandt, B. Brügmann, D. Holz, E. Seidel, R. Takahashi and J. Thornburg, gr-qc/9908012.

18) M. Shibata, Prog. Theor. Phys. **101** (1999), 1199.

19) M. Shibata, T. W. Baumgarte and S. L. Shapiro, Phys. Rev. **D61** (2000), 044012.

20) W. H. Press, B. P. Flannery, S. A. Teukolsky and W. T. Vetterling, *Numerical Recipes* (Cambridge University Press, 1989).

21) B. J. van Leer, J. Comp. Phys. **23** (1977), 276.

22) Even if we solve Eq. (2·13) using the Γ-law equation of state, the equation of state is preserved in polytropic form with invariant K in the case that we do not add artificial viscosity in our present choice of the energy equation. This is because the relation $e_*/\rho_* = \{P/(\Gamma-1)\}^{1/\Gamma}/\rho =$constant holds during the evolution in the absence of the artificial viscosity.

23) R. F. Stark and T. Piran, Comp. Phys. Rep. **5** (1987), 221.

24) G. Cook, S. L. Shapiro and S. A. Teukolsky, Phys. Rev. **D53** (1996), 5533.

25) For example, H. Komatsu, Y. Eriguchi and I. Hachisu, Mon. Not. R. Astron. Soc. **237** (1989), 355.
G. Cook, S. L. Shapiro and S. A. Teukolsky, Astrophys. J. **398** (1992), 203.
S. Bonazzola, E. Gourgoulhon, M. Salgado and J.-A. Marck, Astron. Astrophys. **278** (1993), 421.

26) G. Cook, S. L. Shapiro and S. A. Teukolsky, Astrophys. J. **422** (1994), 227.

27) M. Shibata, T. W. Baumgarte and S. L. Shapiro, Astrophys. J. **542** (2000), in press, astro-ph/0005378.

28) We note that even if $K^{-1/2}$ is smaller than 3.6, a black hole could be formed for the case in which the gravitational binding energy is sufficiently large initially. Hence, the value 3.6 is not an absolute threshold, even for $q = 0$, although it could be a good guideline.

29) We reached this conclusion because convergence was not well achieved when N was increased.

30) Throughout this paper, ρ_c and ρ $(r = 0)$ are used as the central density at $t = 0$ and the central density during the time evolution, respectively. $\rho_{\max}$ denotes the maximum density at $t = 0$.

31) N. Stergioulas and J. L. Friedman, Astrophys. J. **492** (1998), 301.

32) T. W. Baumgarte, S. L. Shapiro and M. Shibata, Astrophys. J. Lett. **528** (2000), L29.

33) Note that q of a formed black hole is expected to be ~ 0.9 in this case. This implies that the coordinate radius of the innermost stable circular orbit around the black hole is $\sim 2M_g$ in our coordinate systems, and hence, matter located at $\gtrsim 2M_g$ could maintain a stable orbit.

34) For example, S. L. Shapiro and S. A. Teukolsky, *Black Holes, White Dwarfs, and Neutron Stars* (Wiley Interscience, New York, 1983), chapter 12.

35) S. Yamada and K. Sato, Astrophys. J. **434** (1994), 268.